



저작자표시-비영리-변경금지 2.0 대한민국

이용자는 아래의 조건을 따르는 경우에 한하여 자유롭게

- 이 저작물을 복제, 배포, 전송, 전시, 공연 및 방송할 수 있습니다.

다음과 같은 조건을 따라야 합니다:



저작자표시. 귀하는 원저작자를 표시하여야 합니다.



비영리. 귀하는 이 저작물을 영리 목적으로 이용할 수 없습니다.



변경금지. 귀하는 이 저작물을 개작, 변형 또는 가공할 수 없습니다.

- 귀하는, 이 저작물의 재이용이나 배포의 경우, 이 저작물에 적용된 이용허락조건을 명확하게 나타내어야 합니다.
- 저작권자로부터 별도의 허가를 받으면 이러한 조건들은 적용되지 않습니다.

저작권법에 따른 이용자의 권리는 위의 내용에 의하여 영향을 받지 않습니다.

이것은 [이용허락규약\(Legal Code\)](#)을 이해하기 쉽게 요약한 것입니다.

[Disclaimer](#)

공학박사학위논문

액체 금속과 금속 나노와이어 기반  
가변적 전기적 물성을 가진  
레이저 유도 금속성 2상 복합체

Laser-Induced Biphasic Metallic Composite  
with Adjustable Electrical Properties  
using Liquid Metal and Metallic Nanowires

2023 년 02 월

서울대학교 대학원  
기계공학부

조철민

액체 금속과 금속 나노와이어 기반  
가변적 전기적 물성을 가진  
레이저 유도 금속성 2상 복합체

Laser-Induced Biphasic Metallic Composite  
with Adjustable Electrical Properties  
using Liquid Metal and Metallic Nanowires

지도교수 고 승 환

이 논문을 공학박사 학위논문으로 제출함  
2022년 10월

서울대학교 대학원  
기계공학부  
조철민

조철민의 공학박사 학위논문을 인준함  
2022년 12월

위원장 박용래 (인)

부위원장 고승환 (인)

위원 이호원 (인)

위원 홍석준 (인)

위원 권진형 (인)

**Ph.D. Dissertation in Mechanical Engineering**

**Laser-Induced Biphasic Metallic  
Composite with Adjustable Electrical  
Properties using Liquid Metal and  
Metallic Nanowires**

**액체 금속과 금속 나노와이어 기반 가변적 전기적  
물성을 가진 레이저 유도 금속성 2상 복합체**

**February 2023**

**Graduate School of Mechanical Engineering  
Seoul National University**

**Chulmin Cho**

# **Abstract**

## **Laser-Induced Biphasic Metallic Composite with Adjustable Electrical Properties using Liquid Metal and Metallic Nanowires**

Chulmin Cho  
Department of Mechanical Engineering  
The Graduate School  
Seoul National University

The rapid advancement of science and technology has led to the exploration of stretchable electronics, which have numerous potential applications in areas such as biology, energy, and soft robotics. Stretchable electrodes, a key component of stretchable electronics, have been the focus of extensive research from both material and process perspectives. At the same time, novel applications based on these electrodes have also been proposed.

This dissertation presents the development of stretchable electrodes using liquid metals and nanowires as materials and lasers as a process. While previous studies have utilized only one property of either liquid metals or nanowires, the dissertation combines the unique liquid properties of liquid metals with the conductive structure of nanowires as a 1D material to control the degree of entanglement of the two substances using laser equipment. This resulted in the creation of a metallic biphasic (solid-liquid) composite that can control electrical properties and also has the

potential for use as a heater. In addition, the dissertation introduces a novel vacuum filtration transferring method for producing uniform liquid metal electrodes. Furthermore, the Monte Carlo simulation for the mixture of liquid metal particles and nanowires in the dissertation provides a solid foundation for future research in this field.

**Keywords:** Liquid metal  
Metallic nanowire  
Laser  
Stretchable electrode  
Biphasic metallic composite  
Varying properties

**Student Number:** 2019-35256

# Table of Contents

<b>Abstract .....</b>	<b>i</b>
<b>Table of Contents.....</b>	<b>iii</b>
<b>Chapter 1. Introduction .....</b>	<b>1</b>
<b>1.1 Motivation.....</b>	<b>1</b>
<b>1.2 Research scope and overview .....</b>	<b>3</b>
<b>1.3 Dissertation layout.....</b>	<b>7</b>
<b>Chapter 2. Literature Review.....</b>	<b>8</b>
<b>2.1 Stretchable electronics from a material perspective .....</b>	<b>8</b>
2.1.1 Bulk liquid metal .....	8
2.1.2 Liquid metal particle and composite .....	11
2.1.3 Metallic nanowire.....	13
<b>2.2 A study on a laser from a process perspective .....</b>	<b>14</b>
2.2.1 Classification according to the laser pulse length .....	14
2.2.2 Laser-derived effects and applications .....	15
<b>Chapter 3. Fundamental Study on Material and Laser Process .....</b>	<b>17</b>
<b>3.1 Liquid metal.....</b>	<b>17</b>
3.1.1 From bulk liquid metal to liquid metal particle.....	17

3.1.2	Development of laser based liquid metal patterning framework.....	20
<b>3.2</b>	<b>Introduction of additional material to EGaInPs .....</b>	<b>25</b>
3.2.1	Copper plate and copper nanowire .....	25
3.2.2	Silver nanowire.....	26
<b>Chapter 4.</b>	<b>Fabrication of Uniform Liquid Metal Film .....</b>	<b>34</b>
<b>4.1</b>	<b>Necessity of uniform film for laser processing.....</b>	<b>34</b>
<b>4.2</b>	<b>Introduction of vacuum filtration technique .....</b>	<b>37</b>
<b>4.3</b>	<b>An effort to increase the yield of the liquid metal film.....</b>	<b>41</b>
4.3.1	EGaIn particle size .....	41
4.3.2	Amount of AgNW .....	41
4.3.3	Comparison with other mixtures .....	43
<b>Chapter 5.</b>	<b>Simulation of percolation network .....</b>	<b>48</b>
<b>5.1</b>	<b>Percolation theory and Monte Carlo simulation .....</b>	<b>48</b>
<b>5.2</b>	<b>Simulation for defect-free film formation condition .....</b>	<b>49</b>
5.2.1	Numerical modeling for nanowires .....	49
5.2.2	Consideration of EGaIn particle .....	50
5.2.3	Verification and validation of simulation with experiment result .....	52
<b>Chapter 6.</b>	<b>Laser-Induced Biphasic Metallic Composite .....</b>	<b>59</b>
<b>6.1</b>	<b>Entanglement phenomenon .....</b>	<b>59</b>
<b>6.2</b>	<b>Theoretical approach .....</b>	<b>64</b>
6.2.1	Wettability .....	64
6.2.2	Plasmonic effect .....	66

<b>6.3</b>	<b>The degree of entanglement between EGaIn and AgNW</b> .....	<b>69</b>
6.3.1	A quantitative analysis.....	69
6.3.2	Analysis of etching.....	70
6.3.3	Assessment of electromechanical behavior.....	73
<b>6.4</b>	<b>Utilization of LIBMC</b> .....	<b>87</b>
6.4.1	Necessity of the LIBMC heater.....	87
6.4.2	Demonstration of prototype.....	88
<b>Chapter 7.</b>	<b>Conclusions</b> .....	<b>96</b>
7.1	Contributions and significance.....	96
7.2	Suggestions for future research.....	99
<b>References</b> .....		<b>101</b>
<b>국문 초록</b> .....		<b>116</b>

## List of Figures

Figure 1-1	Keywords and scope of the dissertation .....	6
Figure 3-1	Synthesized EGaIn (eutectic gallium-indium alloy).....	21
Figure 3-2	Fabricated EGaInP solution using the stirring method (left) and an optically magnified image of the solution (right).....	21
Figure 3-3	EGaInP solution (left) and thin film from the solution (right).....	22
Figure 3-4	Fabrication of EGaInPs using a tip sonicator.....	22
Figure 3-5	EGaInP solution fabricated using the tip sonication method.....	23
Figure 3-6	Schematic illustration of EGaIn patterning framework.....	23
Figure 3-7	EGaIn patterns on the PDMS substrate. ....	24
Figure 3-8	EGaIn coating on copper foil.....	29
Figure 3-9	No reaction between EGaIn and CuNW film .....	29
Figure 3-10	Schematic illustration of patterning process on the CuNW film ..	30
Figure 3-11	The square-shape EGaIn pattern on the CuNW film .....	30
Figure 3-12	SEM image of transferred EGaInPs with CuNW .....	31

Figure 3-13	Comparison of (i)CuNW and (ii)AgNW with EGaInPs .....	31
Figure 3-14	Sheet resistance according to the amount of AgNW and EGaIn ..	32
Figure 3-15	Before(a) and after(b) laser irradiation to AgNW-EGaInPs mixture .....	33
Figure 3-16	Schematic illustration of stretchable conductor fabrication process .....	33
Figure 4-1	EGaInPs film from (a) drop casting method and (b) spin coating method .....	36
Figure 4-2	Schematic illustration of vacuum filtration and transfer (VFT) method. ....	39
Figure 4-3	Comparison of VFT results for (i)EGaInPs only and (ii) AgNWs- EGaInPs mixture.....	39
Figure 4-4	Thickness of the transferred AgNW-EGaInPs film. ....	40
Figure 4-5	Quality of the transferred EGaInPs film as the average particle size (dp). ....	46
Figure 4-6	Difference of lump debris according to the amount of AgNW. ....	46
Figure 4-7	Sheet resistance data as the amount of AgNW increases.....	47
Figure 4-8	Transferred films through VFT technique on the various substances. .....	47

Figure 5-1	Schematic illustration of a single NW with the coordinate system	54
Figure 5-2	Scattered NWs in the window .....	54
Figure 5-3	NWs (black) and effective NWs (blue) .....	55
Figure 5-4	Definition of the intertwining scope (red circle) .....	55
Figure 5-5	Simulation results based on the number of NWs (100, 200, 500, 1000, 2000, and 4000 EA).....	56
Figure 5-6	A binary plot of extracted intertwining scope based on the number of NWs (100, 200, 500, 1000, 2000, and 4000 EA) .....	57
Figure 5-7	5000 NWs covered 88.9 % of the unit area. ....	58
Figure 6-1	Schematic illustration of principle of the LIBMC formation. ....	62
Figure 6-2	Visualization of calculated energy density.....	62
Figure 6-3	Parametric study results based on the laser power and scanning speed. ....	63
Figure 6-4	Schematic representation of the AgNW-EGaInPs .....	67
Figure 6-5	Result of FDTD simulation at AgNW junction .....	67
Figure 6-6	AgNW-EGaInPs film in high temperature environment. ....	68
Figure 6-7	Laser irradiation to the mixture of bulk EGaIn and AgNWs .....	77

Figure 6-8	Laser irradiation to the mixture of EGaInPs and AgNWs .....	77
Figure 6-9	SEM and EDS for Ga and Ag components in the LIBMC .....	78
Figure 6-10	Relative comparison of XRD data .....	78
Figure 6-11	XRD results of the LIBMC (top) and AgNW-EGaIn film (bottom) .....	79
Figure 6-12	Etching result of LIBMC with SEM images based on the laser intensity.....	80
Figure 6-13	LIBMC electrode before and after etching process.....	80
Figure 6-14	Schematic illustration of the selective laser patterning and etching in the AgNWs-EGaInPs film. ....	81
Figure 6-15	SEM images for (i) the LM anchoring and (ii) the LM stacking..	81
Figure 6-16	LIBMC conductor: (i) computer-aided drawing, (ii) prototype, and (iii) grid.....	82
Figure 6-17	Direct laser patterning on various substrates. ....	82
Figure 6-18	Schematic illustration of the laser system.....	83
Figure 6-19	Characteristic profile for Gaussian (left) and flat-top beam (right) .....	83
Figure 6-20	Sheet resistance measurement as a function of laser power before	

	(red) and after (blue) etching. ....	84
Figure 6-21	Relative change in resistance as a function of uniaxial tensile strain on PDMS before etching with various laser conditions. ....	84
Figure 6-22	Relative change in resistance as a function of uniaxial tensile strain on PDMS after etching with various laser conditions. ....	85
Figure 6-23	Cyclic test data for the LIBMC conductor. ....	85
Figure 6-24	Performance assessment by types of the stretchable electrode. ....	86
Figure 6-25	Example of industrial application as electric heater. ....	91
Figure 6-26	Differences of heating wire resistivity by zone. ....	91
Figure 6-27	Conceptual image of LIBMC heater by applying varying conductivity characteristics. ....	92
Figure 6-28	LIBMC heater design and fabricated prototype. ....	92
Figure 6-29	Transient average temperature evolution of the LIBMC heater under zero strain at stepwise voltage rise from 0 to 4 V. ....	93
Figure 6-30	Average temperature for the regions at a constant applied voltage of 4 V under strain variation. ....	94
Figure 7-1	Schematic illustration of crucial points of the LIBMC conductor. ..	98

# Chapter 1

## Introduction

### 1.1 Motivation

In recent years, the field of electronics has seen significant growth in the development of soft, flexible, and stretchable electronics, which have a range of potential applications including soft robotics[1], biomedical sensors[2], wearable devices[3], epidermal electronics[4], and stretchable energy devices[5]. These applications require materials that are compliant with curved surfaces and even living organisms, and have led to the exploration of stretchable conductors such as solid metallic nanomaterials and liquid metals.

Metal nanowire (NW), which is one type of metallic nanomaterials, has emerged as a promising material for stretchable conductors[6]. Compared to bulk metal, NWs arranged as a percolation network exhibit relatively high stretchability characteristics. Recent studies have further improved the stretchability of NW networks by adopting an accordion fan-like percolation network, which not only increases stretchability but also gives it deformation-insensitive properties[7]. Additionally, by intentionally aligning metal NWs, researchers have been able to achieve stretchability over 1000 %[8].

On the other hand, liquid metals (LMs) such as EGaIn (eutectic gallium-indium alloy) have also been investigated as stretchable conductors due to their intrinsic fluidity, deformability, and high electrical conductivity[9, 10]. Researchers have been able to fabricate highly stretchable circuits by connecting rigid components with biphasic EGaIn[11], as well as biocompatible and permeable super-elastic liquid-metal electronic devices using EGaIn and SBS substrates[12].

To further improve stretchable conductors, recent studies have started to investigate the potential of combining the unique properties of NW networks and LMs[13]. For example, by filling the gap between Ag flakes with EGaIn, researchers were able to increase stretchability to 800 %[14]. Additionally, by utilizing the adhesion characteristics between Ag nanoparticles (AgNP) and EGaIn, 3D surface patterning was achieved[15]. These studies demonstrate the potential for combining the unique properties of metal NWs and LMs to create advanced stretchable conductors with improved performance.

Despite recent advancements in the use of NWs, LMs, or a combination of both as stretchable conductors, there are still several key challenges that need to be addressed in order to make them a viable option for next-generation stretchable conductors. One major challenge is the need for an efficient and direct-writing patterning capability that can rapidly adapt to design changes and minimize complex fabrication steps. Additionally, there is a need for the ability to locally control the electrical properties, such as conductivity and gauge factor, in order to create more sophisticated devices that include both electrodes and resistors in a monolithic manner.

While previous studies have focused on improving the performance of stretchable conductors in terms of stretchability and stability, there have been few studies that have addressed these specific challenges. For instance, some studies have focused on changing the conductivity of composites by controlling the composition ratio[16], or varying gauge factors by adjusting structures like mesh arrays[17] or internal porosity[18]. However, these studies have only addressed a single issue and do not involve an efficient technique to locally modulate these properties.

The purpose of this dissertation is to explore the application of laser techniques in the creation of stretchable conductors. These conductors have the potential to overcome existing challenges and improve performance in various fields. The proposed research aims to utilize the unique properties of lasers, such as direct-writing and spatially selective processing[19], to manipulate the properties of NWs and LMs to create stretchable conductors with improved performance. Through this research, it is expected that a deeper understanding of the potential of laser techniques in creating stretchable conductors will be gained, ultimately contributing to the advancement of the field.

## **1.2 Research scope and overview**

The aim of this dissertation is to develop stretchable electrodes by combining LM, NW, and laser. These three main keywords are central contents to the entire dissertation. While each of these has been extensively studied individually by many researchers, recent research has begun to focus on the combination of LM and laser,

as well as NW and laser, respectively. The scope of this dissertation is to bring these three fields together in order to uncover new insights and ultimately make advancements in the field of stretchable electronics. The specific objectives of this research can be divided into two main thrusts:

### **Research thrust 1**

#### **A material perspective approach to investigate the significance of the combined use of LM and NW.**

The field of stretchable electronics has seen significant advancements through the use of LM and NW. Both materials possess unique properties that are highly beneficial for stretchable electronic applications, and as such, have been widely adopted in various research studies. However, recent studies have begun to explore the potential of utilizing a mixture of these two materials to uncover new synergistic effects. The first research thrust of this dissertation is to investigate the interrelationship between LM and NW materials and to explore new results and potential application methods. The current state of the field will be reviewed, highlighting the properties and applications of each material individually. Then, the potential synergistic effects that may be achieved by mixing the two materials, and the methods used to do so, will be delved into. In the experimental section of this dissertation, a series of experiments will be conducted to investigate the interrelationship between the two materials and to explore the new results and potential application methods that may arise from their combination. The results of these experiments will be analyzed and interpreted to provide a deeper understanding of the synergistic effects of the LM and NW mixture.

## **Research thrust 2**

### **A process perspective approach to explore the relationship between laser and the mixture of LM and NW.**

The stretchable electrodes inevitably include a manufacturing process that requires a thorough understanding of the principles behind each application method in order to achieve consistent and desirable results. Even if the same material is used, the results vary depending on the manufacturing process. The second research thrust aims to explore the potential of utilizing a laser process for the manufacturing of stretchable electrodes. The laser process has several advantages, such as the ability to selectively provide heat to a local area and perform the process non-toxically in the room temperature condition. The focus of this study is to utilize these advantages in the combination of LM and NW materials to develop a new stretchable electrode.

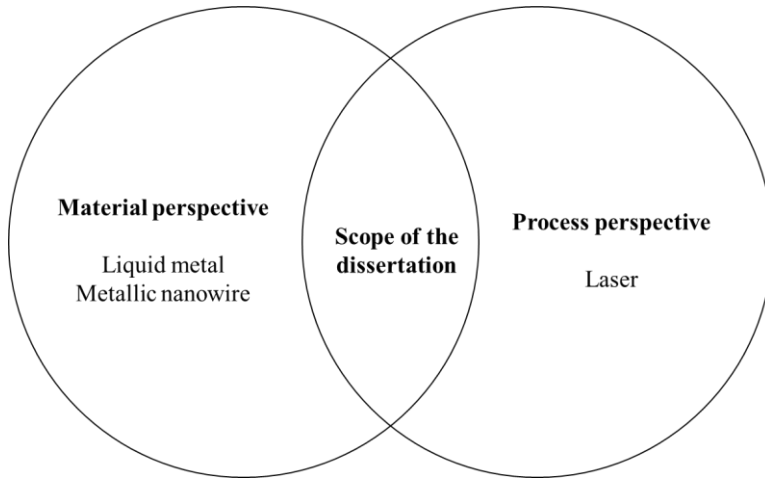


**Figure 1-1 Keywords and scope of the dissertation**

### **1.3 Dissertation layout**

This dissertation is organized into seven chapters, each of which addresses a specific aspect of stretchable electronics from the perspectives of materials and laser processes. Chapter 2 provides a comprehensive review of the literature on stretchable electronics, including the latest developments in LM, NW, and laser processes. Chapter 3 introduces fundamental studies on LM with laser, providing a proposed framework for the dissertation. The chapter also explores the potential challenges and issues associated with the suggested framework and proposes a solution to the issue through the use of NW. Chapter 4 addresses the vacuum filtration transferring (VFT) technique for LM, and explains how the use of NW increases the quality of the transferred film. The chapter also presents experimental results empirically. Chapter 5 analyzes the VFT of LM and NW mixtures based on percolation theory and computational simulation. The chapter also presents a thorough examination of the properties and behavior of these mixtures, and how they can be used in stretchable electronics. Chapter 6 discusses the entanglement effect and laser-irradiated biphasic metallic composite, as well as the characteristics discovered through these studies. This chapter also presents the potential industrial applications of these findings and demonstrates the development of a monolithic heater based on previous research. Finally, Chapter 7 concludes the dissertation by summarizing the contributions and significance of the work, highlighting the key findings and suggesting areas for future research. The dissertation aims to provide a comprehensive understanding of the field of stretchable electronics, and to pave the way for the development of new and innovative technologies in this field.

# Chapter 2

## Literature Review

To develop novel stretchable electronics, it is important to select appropriate materials and apply the right processing techniques. Therefore, it is essential to understand stretchable electronics from both a material and process perspective. This chapter introduces various studies related to LM, NW, and laser. Section 2.1 covers the use of LM and NW as materials for stretchable electronics. Section 2.2 reviews the role of lasers, a key process in this dissertation, in the development of stretchable electronics from a process perspective.

### **2.1 Stretchable electronics from a material perspective**

#### **2.1.1 Bulk liquid metal**

LMs are a class of materials that exhibit metallic properties and are in a liquid state at room temperature[20]. Historically, mercury was the most well-known example of the LM, but due to its poor heat conductivity and potential health hazards associated with exposure, alternatives have been developed. One such alternative is Eutectic Gallium-Indium alloy (EGaIn), a gallium-based LM that has been shown to have improved heat conductivity and electrical conductivity compared to

mercury[21]. Another example is Gallistan, an alloy of gallium, indium, and tin, which also demonstrates improved properties and reduced health risks compared to mercury[22]. With the development of materials, research in this field continues to explore the safe and efficient way of using LMs.

Gallium-based LMs have been widely used in various applications in recent years, including circuits[23], soft actuators[24], sensors[25], and energy devices[26, 27]. Its unique liquid state with non-toxicity has enabled various developments[28]. The fluid property of LM has been further developed and used as a biphasic feature. Hirsch et al. produced an intrinsically stretchable thin film using the biphasic (solid-liquid) nature of LM[9]. However, despite its advantageous properties, LM is often difficult to use due to its high surface tension[29]. To overcome this limitation, researchers have explored various approaches to achieve the desired patterns. Microfluidic-based electronic devices using microchannel injection techniques have been developed for decades due to their simplicity and intuitiveness[30]. Another intuitive approach is the stencil printing technique. Hao et al. fabricated LM on hydrogel using a stencil printing technique[31], which creates strong hydrogen bonds between the oxidized gallium and the hydroxyl groups of the hydrogel[32, 33]. The rapid development of 3D printing technology has also enabled the intuitive direct writing of LM[34]. This method has been used to create not only planar patterns[35] but also non-planar or vertical patterns[36]. Pan et al. used laser ablation to study the direct writing of LM, leaving only the desired parts and removing the rest[37]. In addition to intuitive techniques, the material characteristics of gallium-based LM and other substances have led to new patterning techniques. EGaIn, the most widely used gallium-based LM, is known for its strong bond with gold. DeJace

et al. used this property to create microscale LM conductors with the help of a gold-sputtered PDMS substrate[38]. Other approaches to creating stretchable LM patterns through the fab process have also been developed for sophisticated digital patterns[39]. Kim et al. achieved a sub-micron design with a minimum size of 180 nm and a line spacing of 1  $\mu\text{m}$  by combining the gold-EGaIn contact properties and fab processes[40]. Krisnadi et al. developed a simple but novel approach based on dielectrophoresis, rheology, and electromagnetics[3, 41]. Adding materials to bulk LM has also been explored as a way to discover new properties. Bio-friendly soft electrodes have been developed by combining hydrogel and LM[42]. Chang et al. created recoverable LM paste by mixing quartz powder with LM[43]. A fast-response water-triggered material was also discovered using aluminum, sodium hydroxide, and LM[44]. Copper has been used in the transitional state metallic amalgam[45] and interactive skin electronics[33].

LM patterning has been studied for various applications, including stretchable electrodes, connectors, and fibers. Liu et al. reported the development of extremely stretchable multilayer electronic circuits using LM, with tensile stretchability of over 1000%[46]. Yun et al. used a LM electrode to connect bifacial perovskite solar cells and heaters[47], and all-soft supercapacitors based on LM electrodes have been fabricated[48]. The use of EGaIn-metal interfaces for versatile connectors, such as in microelectronics integration, has also been investigated[49]. In addition, LM-based fibers have been developed, which can be used for multi-purpose textiles and clothes[50, 51]. These fibers are able to change shape, enabling their use in a variety of applications[52, 53].

### **2.1.2 Liquid metal particle and composite**

Bulk LM has been the subject of significant research due to its excellent electrical and thermal conductivity properties. Furthermore, there has been a growing interest in LMs that have been functionalized by altering their morphology as particles[54]. Compared to bulk LMs, LM particles are more susceptible to the formation of a native oxide shell, due to the increased surface area to volume ratio. As a result, LM particles exhibit unique characteristics such as surface modification, sintering, and the ability to be precisely tuned in size[55, 56]. These properties make LM particles an attractive material for various applications.

Several studies have been conducted utilizing the unique properties of LM particles. For example, Lin et al. fabricated hand-writable soft antennas using LM particles[57]. The hand-writable characteristics have been developed as a tattoo applied directly to the skin[58]. Additionally, studies focusing on gallium oxide shells have been investigated to reveal additional functionality. Tang et al. examined the fundamental and technological aspects of the solidification process of gallium oxide layers[59]. Advances in LM surfaces have also led to the development of ligand-treated or core-shell structure LM particles[60, 61]. Furthermore, LM particles have been utilized as initiators for reactions[62, 63]. Not only have many studies aimed to alter the properties of LM particles at room temperature, but changes in response to different temperature conditions have also been reported. Cutinho et al. observed that the surface features of the gallium oxide shell changed under different temperature conditions[64]. Furthermore, the combination of LM particles with other materials has been a subject of recent research. For instance, a stretchable electrode was fabricated using an inkjet printer that utilized both LM

particles and silver nanoparticles [65]. The collaboration of EGaIn particles and Ag flakes has led to a breakthrough in electromechanical behavior[14]. Additionally, a functional electrode sintered by evaporation was developed using a combination of biological nanofibrils and LM particles[66]. These studies demonstrate the potential of LM particles to be used in conjunction with other materials to create new and unique functionalities.

Also, the emergence of LM composites, which are material systems composed of LM alloys, such as EGaIn, suspended as nano or micro-scale droplets within a polymer matrix or mixed with metallic particles to form a biphasic composition led to a significant shift in the field of stretchable electronics, as they exhibit unique electrical, dielectric, and thermal properties. Studies have demonstrated that LM composites can be used to enhance the performance of various electronic devices and systems, including sensors, actuators, and energy storage systems[67, 68]. For example, Neumann et al. achieved direct writing printing of a self-encapsulating LM–silicone composite by simply mixing PDMS and EGaIn. The suspension of EGaIn particles formed electrical pathway in polymer matrix[69]. The polymer called as LM embedded elastomer (LMEE) was suitable for connecting target objects including thermoelectric generators[70]. Biphasic characteristics of LMEE enabled not only self-healing LM-elastomer composite [71] but also active control of insulator-conductor[72, 73]. Biphasic LM composites assisted with ag flakes were used for sinter-free stretchable electronics[74]. Park manufactured LMEE using sugar to increase the surface area in a porous form to use as a self-powered motion sensor[75]. LMEE studies have also been reported to improve performance by mixing graphene flakes [76] or silver flakes[77]. Likewise, mixing LM with other

materials makes the unique properties of each material available. LM-gelatin hybrids were utilized as anisotropic conductive films with self-healable and recyclable properties[78]. Conducting LM hydrogel is suitable for biomedical devices since the non-toxic properties of LM and hydrogels[79, 80]. Further from here, LM particles were used to initiate and further cross-link polyacrylic acid (PAA) chains into a liquid-free polymeric network without any extra initiators and cross-linkers for the multifunctional ionic conductive elastomer[81]. Overall, the use of LM particles has led to the development of a range of unique materials with a variety of potential applications.

### **2.1.3 Metallic nanowire**

Nanowires are structures with a diameter in the nanometer range and an aspect ratio of about 1000:1[82]. They possess 1D structures that allow for quick electron transfer in the longitudinal direction, making them suitable for use as conductors with directional characteristics[83]. These nanowires form intersections, referred to as percolation networks, and are used extensively as major materials for stretchable electrodes. Metal nanowires, including ZnO, AgNW, and CuNW, are utilized in various applications. AgNW is favored for its low metal reactivity [84], while CuNW is used for its cost-effectiveness despite disadvantage of oxidation [85]. Research has also been carried out on core-shell structures that combine these two advantages[86].

Efforts have been made to increase the stretchability of electrodes made of nanowires. This includes synthesizing longer nanowires[87], changing their

geometric shape [7], or the alignment direction of the nanowires during the formation of electrodes[88]. Another approach to simultaneously increasing conductivity and stretchability is welding the junction parts of the nanowires using lasers[89]. Furthermore, regulating the intensity of the laser can be utilized for welding and erasing circuits[90]. Nanowire-based electrodes have been used in a variety of applications, from heater [91], supercapacitor [92] and sensors to deep learning-based temperature and motion prediction technology [93]. These electrodes have evolved over time and continue to do so with technological advancements.

## **2.2 A study on a laser from a process perspective**

### **2.2.1 Classification according to the laser pulse length**

Laser, an acronym for light amplification using stimulated emission of radiation, is a type of artificial light produced by amplifying light using a resonator through the process of stimulated emission. Laser light has a number of unique characteristics, in terms of energy density, coherence, directionality, and monochromaticity[94]. These attributes make lasers useful in a variety of fields, including manufacturing[95, 96], medical[97], industrial[98], and scientific[99] applications. Lasers have been actively utilized in these fields for many years, with numerous studies and articles discussing their use and benefits.

Lasers can be classified into two categories based on pulse length: continuous-wave (CW) lasers and pulsed lasers [100]. CW lasers have a pulse length of 0.25 seconds or more and are used for materials that are not damaged by thermal energy.

These lasers transfer heat to a comparably deep area, enabling micro welding and soldering [101]. Pulsed lasers emit light in the form of optical pulses, as opposed to continuously. This includes picosecond and femtosecond lasers. Pulsed lasers are better suited for processing heat-sensitive or thin materials compared to continuous lasers, as the area affected by heat is more precise and narrow. Using these pulsed laser properties, Yu et al. were able to achieve welding with minimal heat impact using femtosecond lasers[102], and Zhang et al. were able to precisely change the surface from hydrophilic to hydrophobic [103].

### **2.2.2 Laser-derived effects and applications**

The outcome of the laser interaction with the material depends on the the characteristics of the laser. The effect of the laser can be broadly categorized as reduction, enlargement, or deformation of the target object.

The first category of laser-induced reduction encompasses sintering, ablation, and pyrolysis. Lasers generate thermal energy and when a material is exposed to the heat and the temperature exceeds a threshold, it can lead to sintering, which is the process of joining particles together to form a solid mass through a combination of heat and pressure.[104]. Specifically, when the laser irradiates LM particles, the laser beam destroys the oxide shell and allows for easier sintering of the core, resulting in increased electrical conductivity.[105, 106]. Furthermore, laser ablation or pyrolysis is a process of removing material by directing a laser onto a sample surface. It occurs by transferring laser energy to the electrons on the material's surface, causing heating and vaporization of the material, leading to the creation of a high-temperature

plasma.[107]. As energy input continues, the plasma density increases, producing shock waves and solid exfoliation through phase explosion, leading to ablation. Several studies have reported successful circuit patterning using the principle of ablation.[49, 108]. Also, pyrolysis can be used to achieve monolithic digital patterns through facile laser processing on polyimide[109] and PDMS substrates[110].

The second category of laser-induced enlargement effect includes additive manufacturing[111], a process of creating a structures by 3D structuring[112], micromachining[113], and direct writing[114]. 3D structuring involves building a desired 3D shape through layering or carving materials. Micromachining involves producing diverse shapes by modifying materials in a microscopic scope. Direct writing refers to fabricating a desired structure by selectively depositing and removing material.

Finally, laser-based functional surface coating and deposition techniques, such as selective reduction of materials[115, 116] or the fabrication of laser-induced graphene[117, 118], are used to form a layer with a different material on the substrate in order to supplement the material's function or provide additional special functions. These techniques, known as coating or deposition, involve the process of adding a layer to the material's surface. In manufacturing and industrial fields, laser-based coatings and depositions are often used to improve surface hardness, prevent corrosion, increase thermal resistance, and enhance abrasion resistance.

# Chapter 3

## Fundamental Study on Material and Laser Process

This section proposes a framework for stretchable electrodes through a fundamental study of LM and metallic NWs with laser irradiation. Section 3.1 explores the fabrication of stretchable electrodes using only LM and laser. Section 3.2 propose an improved process by suggesting a mixture of LM and metal NWs.

### 3.1 Liquid metal

#### 3.1.1 From bulk liquid metal to liquid metal particle

In the dissertation, EGaIn was selected for study from several LMs and was synthesized for use. The manufacturing recipe is as follow. Gallium (Ga, 99.99 %) and indium ingot (In, 99.99 %) were purchased from ROTOMETALS. First, gallium was put into a convection oven. After solid gallium turned into a liquid state, 75.5 wt% of gallium and 24.5 wt% of indium were put into a beaker together. Afterward, the beaker was heated at 200 °C with 100 rpm of magnetic stirring for 24 hours. Figure 3-1 shows manufactured EGaIn. EGaIn has a low melting point of around

15.6 °C and is often used in electronic and microelectronic applications due to its ability to wet and form a continuous film on a variety of surfaces. However, EGaIn has a high surface tension of 624 mN/m, making it difficult to fabricate thin films without specific design considerations. Previous studies have used EGaIn in conjunction with copper to fabricate thin films. However, the dissertation will explore a different approach to fabricating a thin and uniform LM film in order to be used on various substrates.

To fabricate a thin film of EGaIn, it is necessary to overcome the surface tension of the alloy. One way to do this is to use EGaIn particles (EGaInPs) that are surrounded by a solid oxide shell. When EGaIn is exposed to oxygen in the air, it will form an oxide layer on its surface as a result of the reaction between the metal and oxygen. This oxide layer, also known as the gallium oxide shell, can protect the underlying EGaIn from further oxidation and help to preserve the liquid-like properties of the alloy. This can make it easier to handle and manipulate the EGaIn, and can also help to improve the performance and stability of devices made with the alloy. To manufacture EGaInPs, magnetic stirrer was used as first step. The recipe for this method is as follows: 10 ml of ethanol and 1 ml of gallium are placed in a 20 ml vial, and a magnetic stirrer is added. The mixture is stirred at a speed of 300 rpm for 24 hours. The results of this method may vary slightly depending on the speed of the stirrer and the length of stirring time, but these differences are generally minimal. Figure 3-2 illustrates the EGaInPs solution obtained through the stirring method. As shown in the figure, the solution in the vial is separated into two layers. To understand the cause of this separation, the solution was examined under an optical microscope. The microscopy revealed the presence of EGaInPs ranging in size from

approximately 100  $\mu\text{m}$  to particles that were not distinguishable by the microscope. The presence of these particles in two layers, with the larger particles sinking to the bottom and the smaller particles floating at the top, can lead to issues in the manufacture of thin films with uniform thickness. The variation in particle size can result in non-uniformity in the resulting thin film. Figure 3-3 shows a fabricated EGaInPs film by using the previously synthesized EGaInP solution. The solution was applied to a glass surface using the Mayer rod method to fabricate a thin film. Upon observation, the large particles in the film were visible and had a shining silver metallic color. The uniform thickness of the EGaInP film is an important factor in achieving consistent results during the laser process, as the laser irradiation results can vary based on the smoothness of the surface and the focal distance. However, the magnetic stirring method was not successful in producing a uniformly thick film and was therefore not adopted. Thus, the use of a tip sonicator was newly employed in order to achieve a more uniform particle size. This technique utilizes high frequency sound waves, which are directed through a small nozzle, or "tip," that is immersed in the solution. As the sound waves propagate through the solution, they generate intense pressure waves that cause the particles to collide and aggregate, resulting in a more homogenous distribution of particles. Additionally, the tip sonicator has been shown to be an effective means of breaking up aggregates and dispersing particles, further contributing to the uniformity of the solution. The recipe for this method is as follows: 8 ml of EGaIn are placed in a beaker containing 80 ml of ethanol, and the beaker is immersed in an ice-water bath. The tip sonicator (UH-1200Z with a  $\Phi 13$  mm probe, manufactured by Fangke Technology (Shanghai) Co., LTD.) is then used to sonicate the mixture for 15 minutes (1 minute of operation followed by 1 minute of rest, repeated eight times, with the power setting at 95%).

Figure 3-4 provides a schematic illustration of this method. As shown in Figure 3-5, the EGaInP solution synthesized using the tip sonicator method displayed no separation into layers. This lack of layering suggests that the EGaInPs in the solution are of uniform size. The size of the particles was measured to be in the range of 1 to 10  $\mu\text{m}$ .

### **3.1.2 Development of laser based liquid metal patterning framework**

Thinly spread EGaInP solution on a stretchable substrate was irradiated with a 532 nm continuous wave (CW) laser. The experimental sequence is depicted in Figure 3-6. The process began with the preparation of a PDMS (Polydimethylsiloxane) substrate, which has been widely used in studies due to its stretchability, non-toxicity, and simple fabrication process[119]. However, it can be challenging to spread the EGaInP solution evenly on the PDMS substrate. To overcome the problem, the PDMS substrate was treated with plasma to attach hydroxyl radicals to its surface. The EGaInP solution was then spread on the modified PDMS substrate and selectively irradiated with a laser. Finally, the substrate was immersed in NaOH for etching. This described process represents the laser processing framework used throughout the dissertation. As shown in Figure 3-7, selective patterning was achieved using the EGaInP solution and laser with an etching process. The detailed mechanism of the laser-based design framework will be discussed in Chapter 6. Despite the success of selective patterning, the quality of the resulting pattern was poor. The patterns were faint, and some unintended areas were removed. In order to overcome these issues, efforts were made to improve the pattern quality by incorporating additional materials into the solution.



**Figure 3-1** Synthesized EGaIn (eutectic gallium-indium alloy).

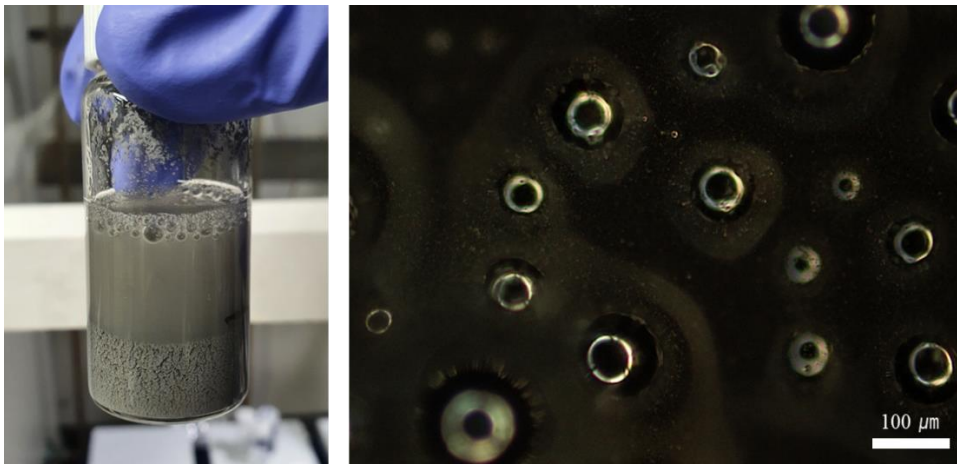


**Figure 3-2** Fabricated EGaInP solution using the stirring method (left) and an optically magnified image of the solution (right).



**Figure 3-3** EGaInP solution (left) and thin film from the solution (right)

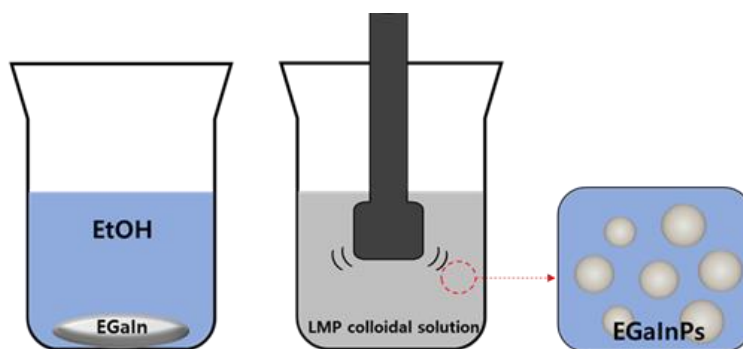


**Figure 3-4** Fabrication of EGaInPs using a tip sonicator.



**Figure 3-5 EGaInP solution fabricated using the tip sonication method.**

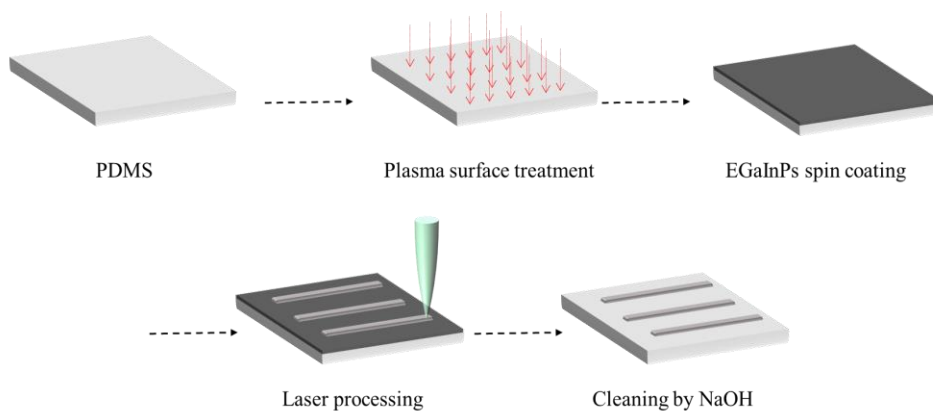


**Figure 3-6 Schematic illustration of EGaIn patterning framework.**

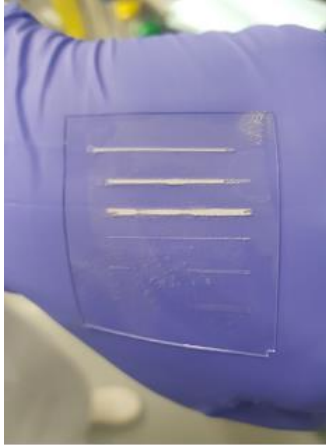


**Figure 3-7 EGaIn patterns on the PDMS substrate.**

## 3.2 Introduction of additional material to EGaInPs

### 3.2.1 Copper plate and copper nanowire

Obtaining clear patterns using a laser and EGaInPs were impossible. In order to improve quality of the pattern, it was proposed to introduce additional material into the EGaInP solution. First, according to the results of the literature research, the quality of the pattern can be improved by utilizing the interrelationship between copper and EGaIn[120]. Figure 3-8 presents the reaction between EGaIn and a copper foil. The EGaIn coating on copper occurs randomly when EGaIn is physically scratched onto the foil using a needle. This phenomenon is occurred due to the transfer of fragments of the gallium oxide shell from the EGaIn to the copper foil [121]. After confirming that bulk copper reacts with EGaIn through the described method, the same approach was applied to CuNWs. This is because while copper foil does not possess stretchable properties, CuNWs have potential as a stretchable electrode due to percolation network. The use of CuNWs in this context allows for the maintenance of the strong binding between copper and EGaIn while also incorporating the stretchable nature of the NWs. However, as shown in Figure 3-9, unlike the copper foil, EGaInPs were not successfully coated onto the CuNW film. This result was caused by the disturbance of the CuNW ligands during the coating process.

Meanwhile, to investigate the reactivity of the CuNW film with a laser, the laser design framework developed in the previous section was applied to the CuNW film, as shown in Figure 3-10. Figure 3-11 presents the patterning results. On the CuNW film substrates, square-shaped EGaInPs were left behind, but the quality of the pattern, particularly the sharpness of the corners, was not sufficient for use. Figure

3-12 shows a SEM image of the pattern, which shows that the CuNWs formed a net-like structure that completely wrapped the EGaInPs to prevent them from leaking out. While this unique structure may be valuable for future research, the fact that the EGaInPs only contacted a single plane of NWs is a weakness for stable patterning. These results prompted the study to move on to using 1D AgNWs (silver nanowires) instead of 2D CuNWs.

### **3.2.2 Silver nanowire**

CuNWs did not react with EGaInPs due to the presence of ligands that prevented oxidation. In contrast, AgNWs, which are more exposed to the metal, were expected to react with EGaInPs. To compare the reactivity of CuNWs and AgNWs with EGaInPs, samples were prepared by mixing each type of NW with the EGaInPs solution, as shown in Figure 3-13. While the CuNW network remained relatively separate from the EGaInPs, the AgNW network formed a lump by intertwining with the EGaInPs. This observation confirmed the feasibility of using 1D AgNWs and their effectiveness in reacting with EGaInPs.

In order to understand the characteristics of the AgNW-EGaInPs mixture when irradiated with a laser, the sheet resistance was measured. Figure 3-14 shows the measured sheet resistance. When the amount of AgNWs is low, the sheet resistance is not measured, even when there is a high density of EGaInPs. Conversely, when the density of EGaInPs is high, the sheet resistance is not measured, regardless of the amount of AgNWs. From these interrelations, a three-dimensional surface graph appears when an appropriate amount of both materials is present. These experimental

results reveal the characteristics of each material: AgNWs are 1D conductors, and EGaInPs are 0D insulators before laser exposure but become conductors after laser exposure. Figure 3-15 compares the effects of laser treatment and non-laser treatment on the AgNW-EGaInPs mixture. Before laser irradiation, the black background is clearly visible. However, after laser irradiation, the background becomes blurred as the EGaInPs fragment and splash. This suggests that the laser caused the EGaInPs to fragment.

A trial to patterning of EGaIn was attempted based on the results of these experiments. The exact method is as follows: First, a 532 nm continuous-wave (CW) diode-pumped solid-state (DPSS) laser (Sprout-G-5W, Lighthouse Photonics) was used to irradiate the prepared AgNW-EGaInPs film on PDMS using a Galvano-mirror (hurrySCAN II, Scanlab). The range of laser power was from 0.25 W to 2 W, and the laser scanning speed was varied from 10 mm/s to 500 mm/s. The laser scanning speed was set to 200 mm/s as the standard, while the laser power was adjusted from 0.5 mW to 2 W. The standard fabrication conditions were determined to be 1.3 W with a scanning speed of 200 mm/s for the direct writing patterning process, which was used to mimic computer-aided drawing patterning. The grid-shaped sample was patterned on various polymer substrates using these conditions. Second, after the laser irradiation process, the film was etched in a 0.2 M NaOH solution for 6 seconds. Finally, the etched film was briefly placed in an ethanol solution to stop the etching process, and then dried on a 60 °C hot plate for 1 minute. Figure 3-16 shows the process and results of laser patterning of the AgNW-EGaInPs mixture. The desired EGaIn patterning was achieved. However, there was a significant issue with yield, as it was difficult to consistently reproduce these results,

even after multiple experiments.

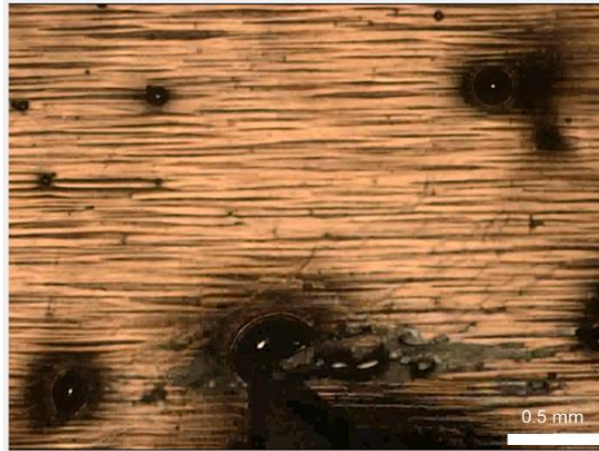


**Figure 3-8 EGaIn coating on copper foil**



**Figure 3-9 No reaction between EGaIn and CuNW film**

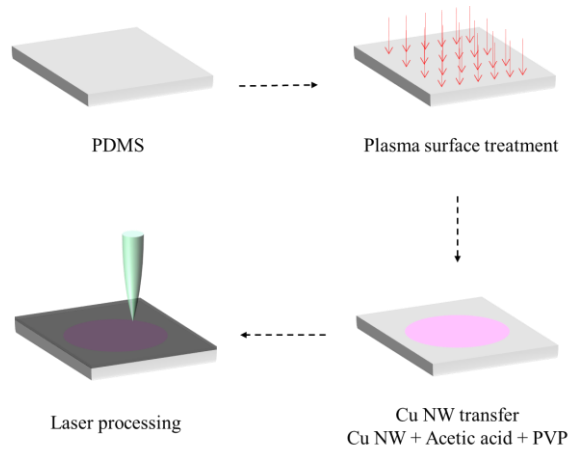


**Figure 3-10 Schematic illustration of patterning process on the CuNW film**



**Figure 3-11 The square-shape EGaIn pattern on the CuNW film**

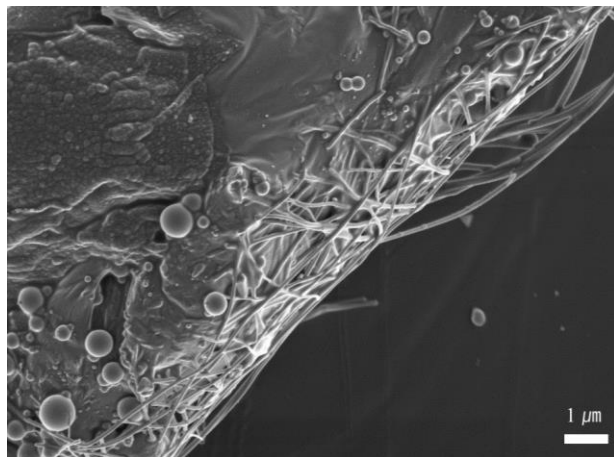


Figure 3-12 SEM image of transferred EGaInPs with CuNW

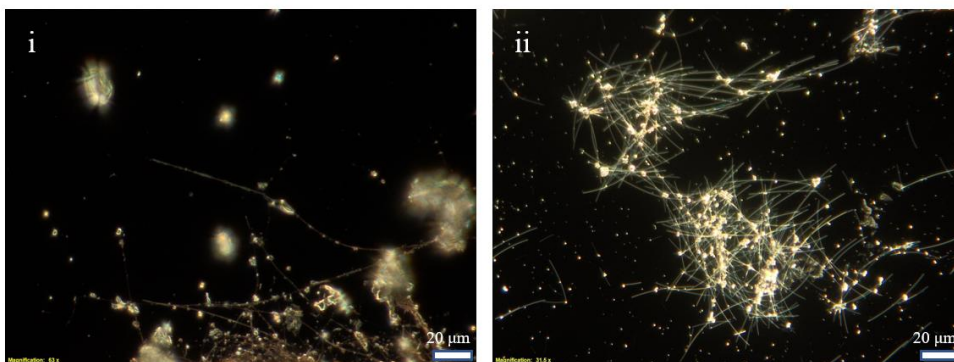


Figure 3-13 Comparison of (i)CuNW and (ii)AgNW with EGaInPs

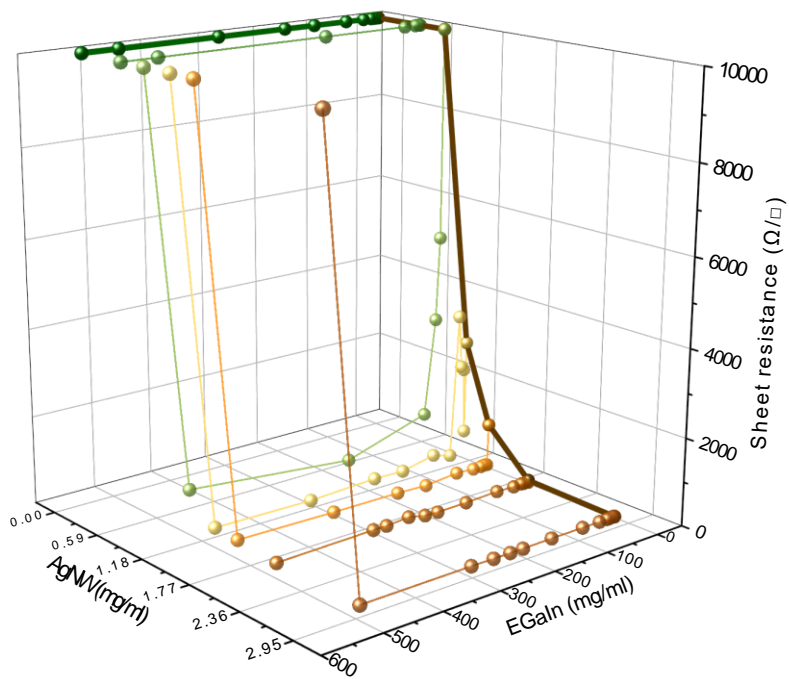
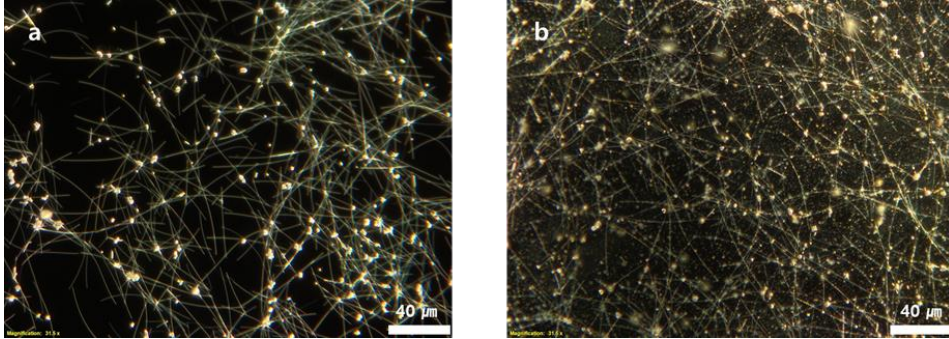
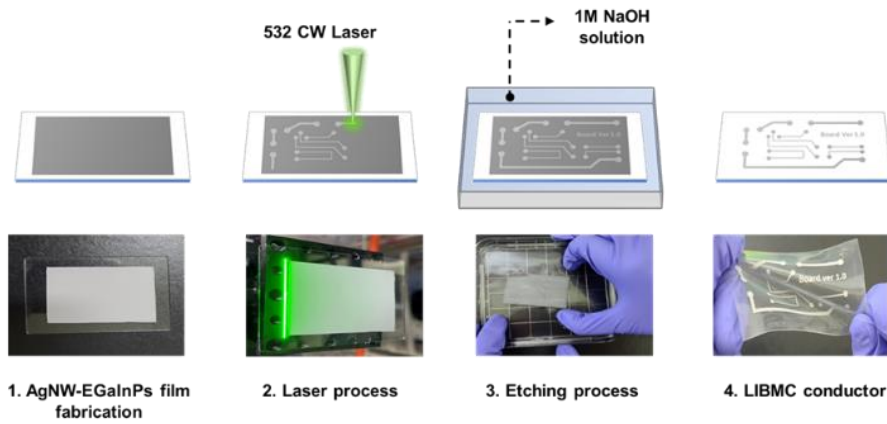


Figure 3-14 Sheet resistance according to the amount of AgNW and EGaIn



**Figure 3-15** Before(a) and after(b) laser irradiation to AgNW-EGaInPs mixture



**Figure 3-16** Schematic illustration of stretchable conductor fabrication process

## **Chapter 4**

# **Fabrication of Uniform Liquid Metal Film**

This section describes the fabrication of LM thin film. Section 4.1 discusses the need of fabricating a film with uniform thickness for the laser process. Section 4.2 lists methods commonly used to fabricate thin films and explains why the mentioned methods are unsuitable for LMs. Section 4.3 introduces a vacuum filtration transfer (VFT) method which is suitable for LM film fabrication.

### **4.1 Necessity of uniform film for laser processing**

The quality of fabricated stretchable LM electrodes in Chapter 3 did not meet the expectation, likely due to the colloidal properties of the EGaInPs solution. EGaIn has a density of 6.25 g/ml and EGaInPs have a diameter range of 1 to 10  $\mu\text{m}$ , making it difficult to use traditional coating methods such as Mayer rod coating or spin coating on EGaInP solutions. Figure 4-1 presents the results of EGaInPs film using the Mayer rod coating and spin coating methods. It is observed that in the Mayer rod coating method, cracks occurred randomly while in the spin coating method, the cracks were limited to the center of the sample. These cracks, known as desiccation

cracks, formed due to the rapid evaporation of ethanol in areas where the EGaInP solution was more concentrated, leading to uneven drying[122]. The crack regions are susceptible to etching and can also result in non-uniform laser irradiation during the manufacturing process due to variations in surface smoothness and focal distance. As a result, the inconsistent results observed in Chapter 3 was attributed to these factors. To produce a sample with a large area and high yield, it is necessary to ensure a uniform thickness of the EGaInP film.

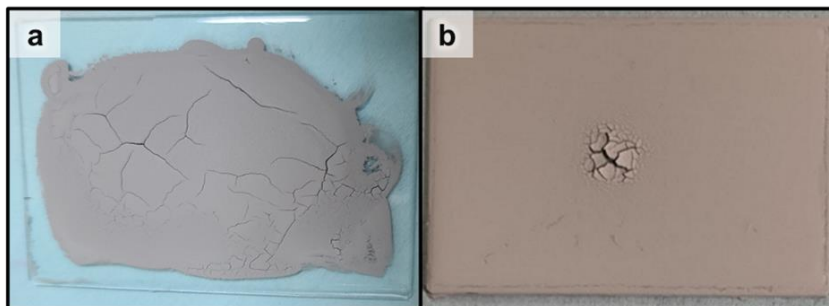


**Figure 4-1** EGaInPs film from (a) drop casting method and (b) spin coating method

## 4.2 Introduction of vacuum filtration technique

In section 4.1, the importance of a uniform thickness of the EGaInP film for consistent results was highlighted. To address this issue, AgNWs will be added to the EGaInP solution to improve its solid properties through the incorporation of both 1D and 0D materials. The material's mechanical properties allowed for the use of the vacuum filtration and transfer (VFT), which is commonly used for fabricating films, has not previously been applied to LMs[123]. VFT used to separate solid nano/micro particles from a solvent solution by trapping the solid particles as a mixture is passed through a filter under the influence of a pressure differential created by a vacuum[124]. The process is illustrated schematically in Figure 4-2. The first step is to prepare a stretchable PDMS substrate by mixing the resin and curing agent in a 10:1 weight ratio (Sylgard 184, Dow Corning), spin coating the uncured PDMS onto glass at 250 rpm for 50 seconds, and curing the PDMS in a conventional oven at 70 °C for 40 minutes. The surface of the cured PDMS is then modified by applying plasma treatment to introduce hydroxy groups. A nylon and polytetrafluoroethylene (PTFE) filter (SterliTech, 47 mm in diameter with a pore size of 0.2  $\mu\text{m}$ ) is placed successively on the funnel. The mixed solution is then poured into a beaker on the Buchner funnel with an additional 100 ml of ethanol and vacuum filtered through the PTFE film. The AgNW-EGaInP solution is then added to the funnel with an additional 100 ml of ethanol. After the solution has passed through the funnel, the prepared PDMS substrate is placed on top and pressed down vertically. The PTFE film is then dried with an air gun and peeled off, transferring the target material onto the PDMS substrate.

The results of VFT before and after the introduction of AgNWs to EGaInPs are

presented in Figure 4-3. As seen in Figure 4-3(i), the film composed solely of EGaInPs is of poor quality and exhibits a stack of spherical 0D structures, which are not suitable for mechanical tangling. In contrast, the introduction of AgNWs as a 1D additive material leads to the formation of stable clusters of EGaInPs, as shown in Figure 4-3(ii). The AgNWs act as a mesh network that confines the EGaInPs, resulting in a clean and stable film that can be transferred to a polydimethylsiloxane (PDMS) substrate via VFT. The thickness of the resulting film, as shown in Figure 4-4, was found to be uniform at 13  $\mu\text{m}$ .

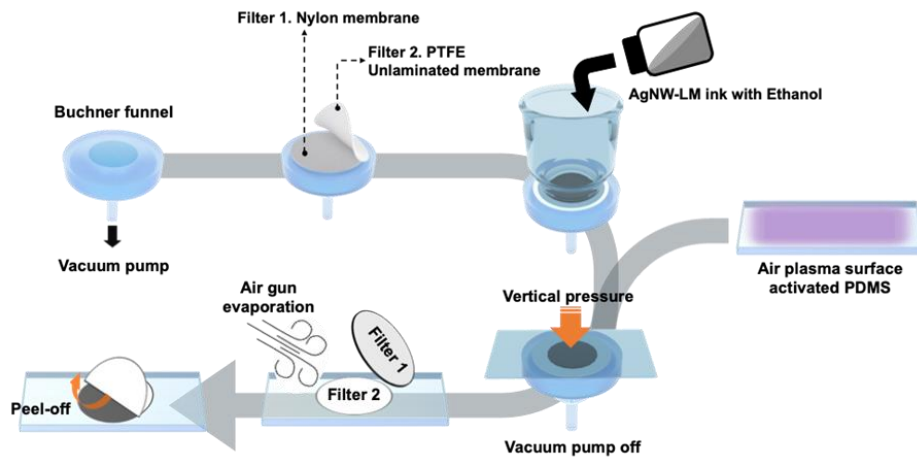


Figure 4-2 Schematic illustration of vacuum filtration and transfer (VFT) method.

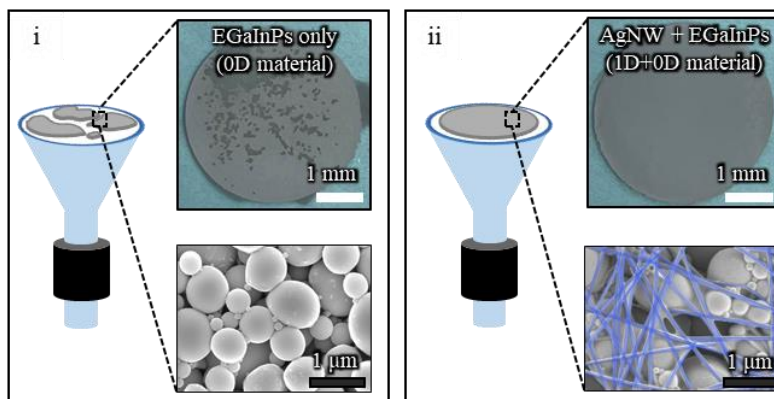
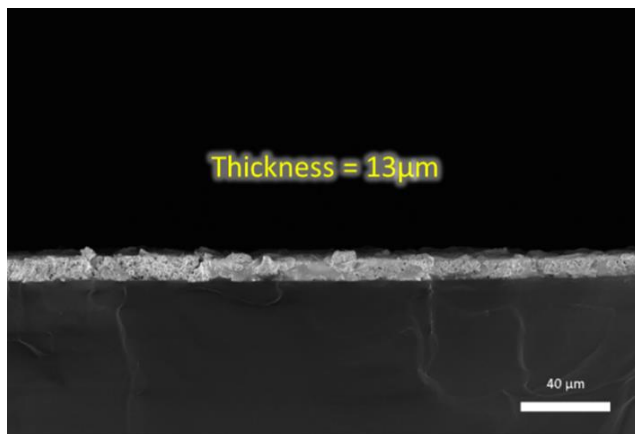


Figure 4-3 Comparison of VFT results for (i)EGaInPs only and (ii) AgNWs-EGaInPs mixture



**Figure 4-4** Thickness of the transferred AgNW-EGaInPs film.

## **4.3 An effort to increase the yield of the liquid metal film**

### **4.3.1 EGaIn particle size**

The ability of EGaInPs to withstand external forces during the VFT process is primarily determined by their size. Figure 4-5 presents the quality of the EGaInPs film according to the particle size. When the diameter of the particles ( $d_p$ ) is larger than 1 mm, they tend to burst under the external forces encountered during the VFT process. Also, particles with diameters between 1  $\mu\text{m}$  and 1 mm maintain their shape, but the bulk EGaIn material may ooze out from the EGaInPs due to mechanical sintering caused by external forces[125]. However, when the particle diameter is small enough (less than 10  $\mu\text{m}$ ), the EGaInPs are able to uniformly form a film structure without experiencing any deformation during the VFT process.

### **4.3.2 Amount of AgNW**

In addition to the size of the EGaInPs, the presence and concentration of AgNWs also have an impact on the results of the VFT process. As discussed in section 3.2.2, EGaInPs and AgNWs play the roles of 0D insulators and 1D conductors, respectively. The inclusion of 1D materials, such as AgNWs, is a crucial factor in determining the quality of the VFT outcomes as they act as a backbone, similar to the intertwining branches of a tree. As the amount of AgNWs increases, the quality of the transferred film improves. This effect can be seen in Figure 4-6, which shows the impact of the tangled AgNW-EGaInP structure on the VFT results. As shown in Figure 4-6(a), there are stains on the right wall of the vial, which are more clearly visible in Figure 4-6(b), where the concentration of AgNWs is increased. This difference in the

entangled branch structure caused by the AgNWs leads to an increase in the film fabrication yield as the concentration density of AgNWs increases.

Figure 4-7 and Table 4-1 describe the effect of the amount of AgNWs on the quality of the film transferred through the VFT technique. Until the amount of AgNW solution is 20  $\mu\text{l}$ , the VFT results are poor, as shown in the inset figures. There are partial holes in the film, and the surface is easily torn off due to the lack of 1D materials, which act as a tangled branch structure. When the amount of AgNWs used reaches 100  $\mu\text{l}$ , the quality of the film reaches its best performance. After several repeated experiments, it was found that at least 50  $\mu\text{l}$  of AgNWs are required for stable film production. Figure 4-7 also illustrates the roles of EGaInPs as 0D insulators and AgNWs as 1D conductors. Until the amount of AgNWs used reaches 15  $\mu\text{l}$ , sheet resistance cannot be measured. When the amount of AgNWs increases to 20  $\mu\text{l}$ , sheet resistance begins to be measured with a wide deviation, following the rule of percolation theory. In this experiment, the density of the AgNW solution was 5.5 mg/ml, and the amount of EGaInPs solution in each case was fixed at 150  $\mu\text{l}$  with a density of 50 mg/ml.

**Table 4-1 Average and standard deviation of measured sheet resistance**

The amount of AgNW	Average (ohm/sq)	Standard deviation
20 $\mu\text{l}$	58.2	20.4
50 $\mu\text{l}$	14.6	4.48
100 $\mu\text{l}$	3.41	0.32

### 4.3.3 Comparison with other mixtures

In order to further verify the role of AgNWs as a backbone due to their 1D structure in creating EGaInP films, a control experiment was conducted using a comparative group including Ag flakes, Ag nanoparticles (AgNPs), copper nanowires (CuNWs), and cellulose. The materials required for the experiment were purchased or synthesized, and the details of the materials are described below.

The silver nanoparticles (AgNPs), silver nanowires (AgNWs), and copper nanowires (CuNWs) were synthesized for this study. The AgNPs were prepared by dissolving 0.25 mol/l of silver nitrate (99% Sigma Aldrich) in ethylene glycol (EG, 99.9%, Sigma Aldrich) with 0.02 mol/L of polyvinylpyrrolidone (PVP,  $M_w \approx 10,000$ ). The solution was stirred at a temperature of 150 °C until the synthesis was complete. The synthesized particles were then separated by centrifugation at 7000 rpm for 30 minutes and washed with ethanol. The collected particles were re-dispersed in ethanol at a concentration of 10 wt%. The AgNWs (100  $\mu\text{m}$  or less in length with a 1000:1 aspect ratio) were synthesized using a modified polyol process. The process involved the simultaneous mixing of all reagents in a triangular flask, resulting in a simple synthesis of NWs. In 50 ml of ethylene glycol (EG), 0.4 g of polyvinylpyrrolidone (PVP,  $M_w \approx 360,000$ ) and 0.5 g of silver nitrate ( $\text{AgNO}_3$ ) were dissolved using a magnetic stirrer. Once all chemicals were completely dissolved, the stirrer was removed from the mixture solution. 800  $\mu\text{l}$  of copper (II) chloride dihydrate solution ( $\text{CuCl}_2 \cdot 2\text{H}_2\text{O}$ , 3.3 mM dilution with EG) were rapidly injected into the mixture and stirred moderately. The mixture solution was then placed in a 130 °C silicone oil bath for 3 hours to complete the growth of the AgNWs. The

resulting solution was cleaned using acetone and ethanol to remove chemical residues, followed by centrifugation at 3000 rpm for 10 minutes three or four times. The purified AgNWs were stored in ethanol as an AgNW solution. The CuNWs were synthesized using a hydrothermal method. 0.84 g of copper (II) chloride dihydrate ( $\text{CuCl}_2 \cdot 2\text{H}_2\text{O}$ , Sigma Aldrich, No. 467847) and 5.2 g of hexadecyl amine (HDA,  $\text{CH}_3(\text{CH}_2)_{15}\text{NH}_2$ , Sigma Aldrich, No. 445312) were dissolved in 400 ml of deionized water in a 500 ml triangular flask and stirred for 24 hours. When the color of the resulting solution turned sky blue, 2 g of glucose (Sigma Aldrich, No. G5767) was added and heated at 10 °C for 7 hours and 20 minutes. After the desired growth was achieved, the solution turned a reddish brown color. The solution was then cleaned using twice the volume of isopropyl alcohol (IPA) with centrifugation for 15 minutes at 1500 rpm. The prepared NWs were stored in IPA for use. In this VFT verification, 450  $\mu\text{l}$  of CuNW solution (density: 1.1 mg/ml), 100  $\mu\text{l}$  of a 10 wt% AgNP solution, 0.1 g of Ag flakes, and 0.1 g of  $\alpha$ -cellulose were used in each case. Commercial  $\alpha$ -cellulose (Sigma Aldrich, No. C8002) and Ag flakes (Sigma Aldrich, No. 327077, 10  $\mu\text{m}$ ) were purchased and used without further treatment.

Figure 4-8 illustrates the results of the control experiment. When Ag flakes and EGaInPs are used together, the quality of the fabricated film is low (Figure 4-8(i)). The tangling in the mixture of Ag flakes and EGaInPs is low, as shown in the schematic figure (inset). The mixture of AgNPs and EGaInPs also produces a poor-quality film (Figure 4-8 (ii)). The size difference between the AgNPs and EGaInPs is disadvantageous for tangling (inset). Although Ag has an affinity with EGaIn, the structure of the 0D and 2D mixture is not advantageous for tangling. Additionally, although CuNWs are 1D materials, the mixture of CuNWs and EGaInPs is not

suitable for fabricating a uniform LM film (Figure 4.8(iii)) because the dense ligand on the surface of the CuNWs prohibits contact between the CuNWs and EGaInPs (inset). In the case of cellulose, the film transferred to the glass collapses due to the mismatch of scale (inset) and the mixture of a non-metallic substance with EGaInPs (Figure 4-8 (iv)).

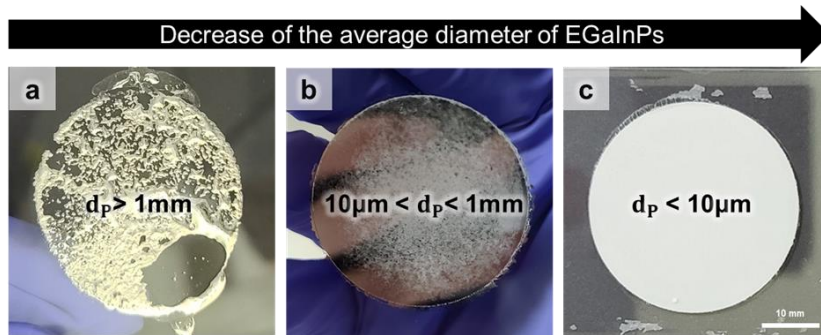


Figure 4-5 Quality of the transferred EGalNPs film as the average particle size ( $d_p$ ).

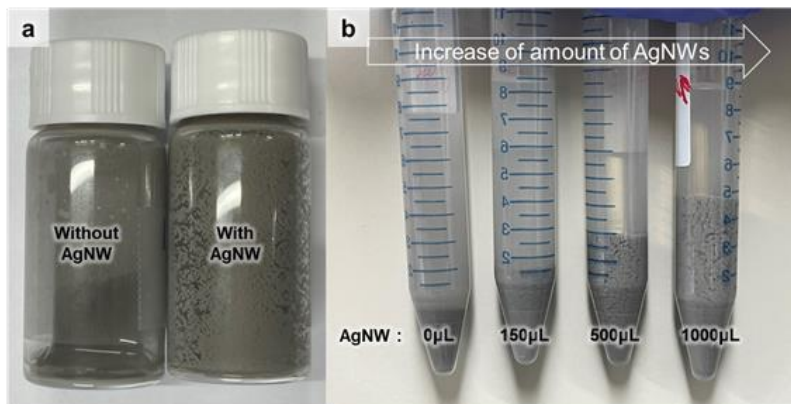


Figure 4-6 Difference of lump debris according to the amount of AgNW.

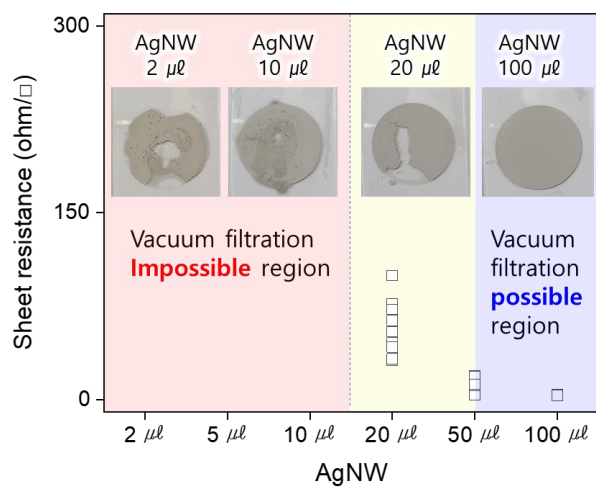


Figure 4-7 Sheet resistance data as the amount of AgNW increases

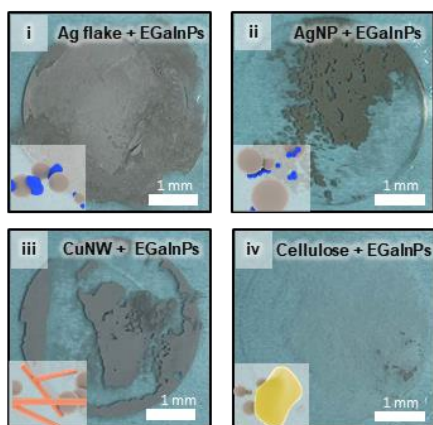


Figure 4-8 Transferred films through VFT technique on the various substances.

## **Chapter 5**

# **Percolation Network Simulation**

Chapter 5 investigates the AgNW-EGaInP film through simulation. While the film production was confirmed through experiments in the previous chapter, a fundamental model and thorough consideration of the formation process has not yet been developed. By performing simulations with mathematical modeling, the chapter aims to determine the conditions under which AgNW-EGaInP films are consistently and adequately formed.

### **5.1 Percolation theory and Monte Carlo simulation**

Percolation theory, which is based on probability, has been used to study the properties of random media[126]. Random media, which are characterized by their porous structure, can be represented as a network. The percolation theory is therefore useful for simulating the geometric properties of such networks. This theory focuses on the behavior at the pore scale, the randomness of porous medium geometry, and the fluid properties of these media. It has a wide range of applications, including geology, hydrology, and fractal mathematics. To understand percolation, simulation technique has been developed.

Monte Carlo simulation is a computational method that uses random numbers to generate random solutions to problems[127]. This nondeterministic approach was first introduced in the 1940s, but has gained widespread use in recent years due to advances in computing power [128]. Monte Carlo simulations are often used to find numerical solutions to complex problems that cannot be solved using analytical models. They have been applied in a variety of fields, including physics and mathematics, and have gained particular attention in the study of percolation networks since the 1990s [129-131]. In the 1970s, Pike and Seager conducted studies on percolation networks in two-dimensional systems [132]. They used Monte Carlo simulations to propose various percolation models for randomly-oriented objects, and developed methods for approximating cluster parameters and solutions. Their approach involved the use of sticks or lines to analyze 2D models of networks based on the length and number of objects. Since their pioneering work, many researchers have developed additional models for understanding porous soil and intertwined NWs, including Englman et al. [133], Charlaix et al. [134], and Robinson et al. [135].

## **5.2 Simulation for defect-free film formation condition**

### **5.2.1 Numerical modeling for nanowires**

To generate a numerical model of NWs, the MATLAB software was utilized. The model is designed to be a 2D representation of the NWs, which are treated as linear structures, simplifying the model by disregarding their curvature. Figure 5-1 shows a schematic illustration of a single NW with a coordinate system. The position and orientation of the NW are randomly distributed, with the center point determining its

shape and position by Assuming a randomly generated NW with coordinates  $(x_i, y_i)$  and rotation angle  $\theta_i$ . The length and diameter of the NW are represented by  $L$  and  $D$ , respectively. Finally, a random NW model is determined by rotating it around the origin along the x-axis and then moving it to the coordinates  $(x_i, y_i)$  generated by the random seed, as shown in equation 5-1.

$$\begin{bmatrix} x_i^1 & x_i^2 \\ y_i^1 & y_i^2 \end{bmatrix} = \begin{bmatrix} \cos \theta_i & -\sin \theta_i \\ \sin \theta_i & \cos \theta_i \end{bmatrix} \begin{bmatrix} -L/2 & L/2 \\ 0 & 0 \end{bmatrix} + \begin{bmatrix} x_i & x_i \\ y_i & y_i \end{bmatrix} \quad 5-1$$

In this dissertation, a numerical model of a random NW is implemented by connecting two nodes. To simplify the analysis, the model assumes that all NWs have an identical length of  $L$ . This assumption deviates from the normal distribution of actual NW lengths. Figure 5-2 illustrates the results of generating 1000 NWs using this model. Additionally, a window with a side length of  $w$  is created to represent the actual distribution of NWs within the lattice of  $w + L$ . This window, represented by a square grid of size  $w \times w$ , serves as a reference for verifying and validating experimental results throughout the study.

### 5.2.2 Consideration of EGaIn particle

In this section, Monte Carlo simulation is conducted under the consideration of interaction between AgNWs and EGaInPs. Through the VFT process of a mixture of AgNWs and EGaInPs, it was observed that the EGaInPs do not separate and

adhere well to the 1D structure of the AgNWs, which is tangled and physically supported. As a result, it is only when two or more NWs become entangled that they were distinguished in blue color, as demonstrated in Figure 5-3. These distinct NWs are referred to as effective NWs.

There are several conditions that must be met for effective NWs and EGaInPs to become entangled. One of these conditions is that the maximum size of the space between NWs must be smaller than the minimum diameter of an EGaInP. Alternatively, the probability of entanglement can be obtained through simulation by generating effective NWs, generating EGaInPs independently and randomly, and then counting the number of EGaInPs that come into contact with the effective NWs. In this dissertation, a straightforward and intuitive simulation approach was used. Figure 5-4 illustrates the simulation assumptions, which involve EGaInPs being caught at the points where effective NWs intersect. The diameter of this region is approximately  $2r$ , where  $r$  is the radius of the EGaInP. This region is referred to as the intertwining scope. The success of AgNW film manufacturing can be

**Table 5-1 Monte Carlo simulation for NW percolation network**

Total number of NWs	Number of NW intersections	Area fraction of total intertwining scope
100	14	0.255 %
500	220	0.879 %
1000	847	4.721 %
2000	3127	15.966 %
3000	7122	40.572 %
4000	12664	82.195 %

numerically evaluated by calculating the ratio of the intertwining scope to the unit area. Figure 5-5 shows the changes in the number of effective NWs and the size of the intertwining scope as the number of NWs increases. The number of NW used, in order, are 100, 200, 500, 1000, 2000, and 4000. When 4000 NW are used per unit area, the intertwining scope can be observed to extend beyond just small dots. For a more accurate representation, unnecessary nanowires and effective NWs were removed, leaving only the intertwining scope. The total area of the intertwining scope was calculated using a binarization technique and software called ImageJ, which converts the image to black and white and calculates the area as shown in Figure 5-6. The results are summarized in Table 5-1, which shows the number and area of intertwining scope generation for each number of NWs used.

### **5.2.3 Verification and validation of simulation with experiment result**

The window size for the simulation was set to 1 mm × 1 mm, and the experiments and simulations were carried out under the same conditions. The NW length used in the experiment was 50 μm and the aspect ratio was 1000:1. In order to verify and validate the experiment and simulation, it is important to know the exact number of NWs per area that were used. The density of the AgNW solution in the experiment was 5.5 mg/ml, and 100 μl of AgNW solution was used during the VFT process. The diameter of the fabricated film was constantly 36 mm and the distribution of AgNWs was even. The loss factor was assumed to be 10%, considering the state in which EGaIn and AgNW are tangled together in a mixture state and the thickness of the fabricated film. Under these conditions, there are approximately 0.054 μg of AgNW per 1 mm<sup>2</sup> of the unit window in one plane. On the other hand, assuming that the

AgNWs have a cylindrical structure, the volume of a single NW can be calculated as approximately  $0.1 \mu\text{m}^3$  based on the given length and aspect ratio. The weight of a single NW can then be calculated as  $1.05 \times 10^{-12} \text{ g}$  using the density of Ag, which is  $10.49 \text{ g/cm}^3$ . Combining these values, there are approximately 50000 NWs in the unit window. The previous simulation showed that a stable plane begins to form when there are as few as 4000 NWs per  $1 \text{ mm}^2$ . The simulation results confirm that the concentration and number of NWs used in the experiment were sufficient to produce a stable film.

However, the simulation also shows that more than  $10 \mu\text{l}$  of AgNW solution is needed to fabricate a defect-free film, as shown in Figure 4-7. This corresponds to approximately 5000 NWs based on the previous calculation method. The simulation results using 5000 NWs, shown in Figure 5-7, indicate that there is a probability of an area occupied by around 11 %. This value can be taken as the critical value based on the number of NWs needed to manufacture a flawless film. In conclusion, the relationship between the simulation and the experiment allows for prediction through the simulation. For example, even if the length and aspect ratio of the NWs change during synthesis, the exact amount of usage can be predicted using the simulation.

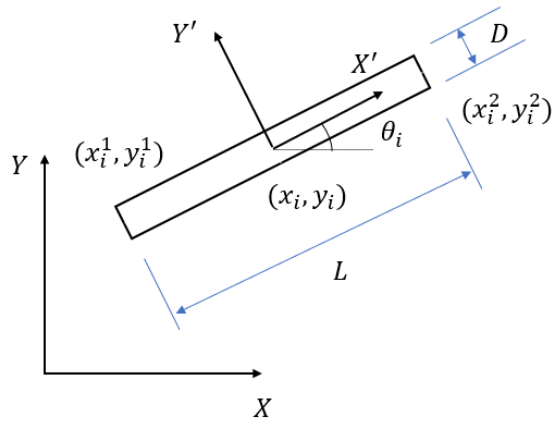


Figure 5-1 Schematic illustration of a single NW with the coordinate system

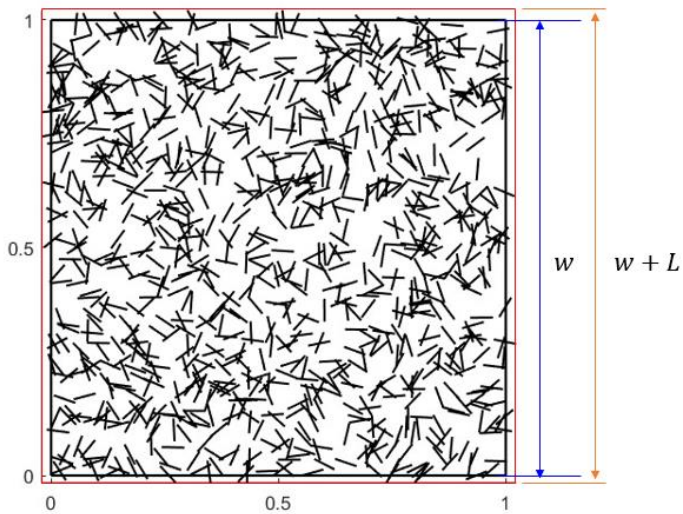
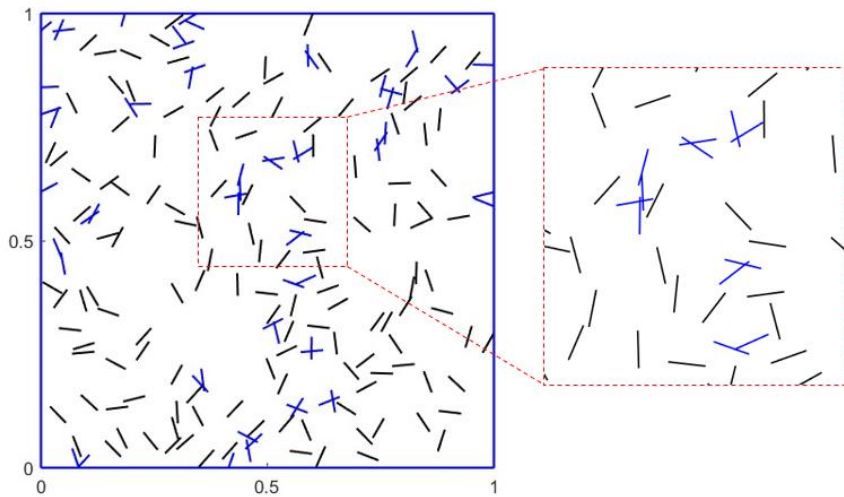
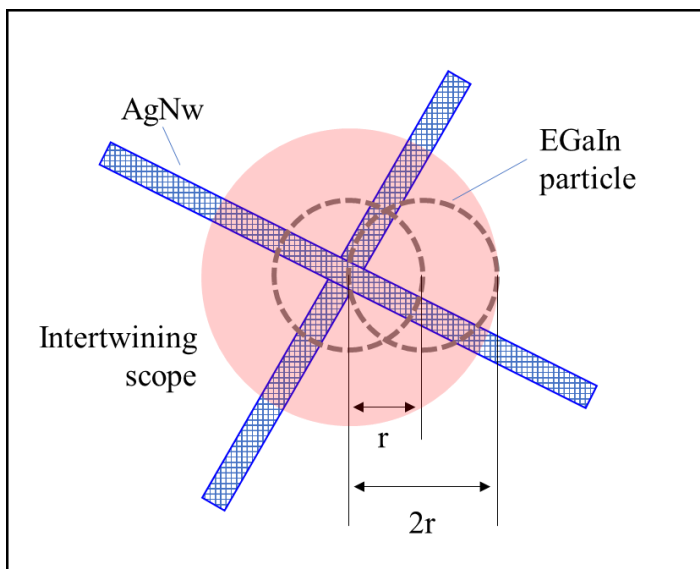


Figure 5-2 Scattered NWs in the window



**Figure 5-3** NWs (black) and effective NWs (blue)



**Figure 5-4** Definition of the intertwining scope (red circle)

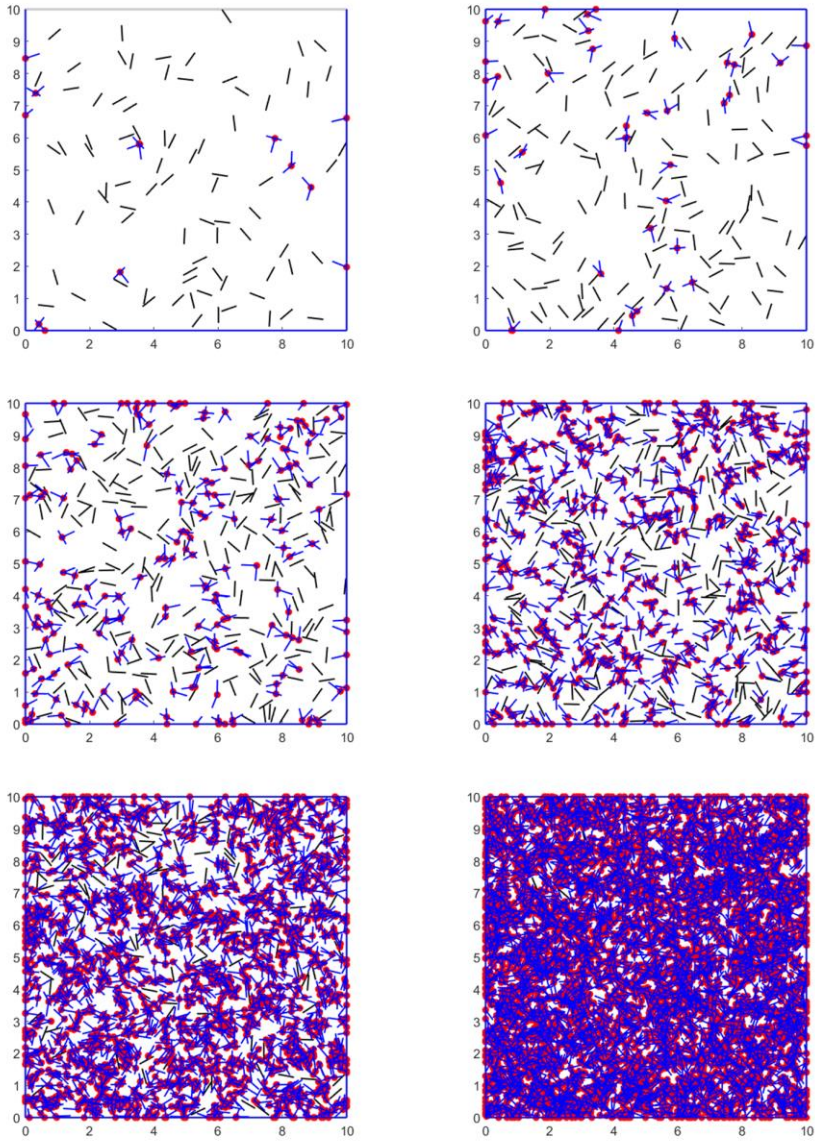


**Figure 5-5 Simulation results based on the number of NWs (100, 200, 500, 1000, 2000, and 4000 EA)**

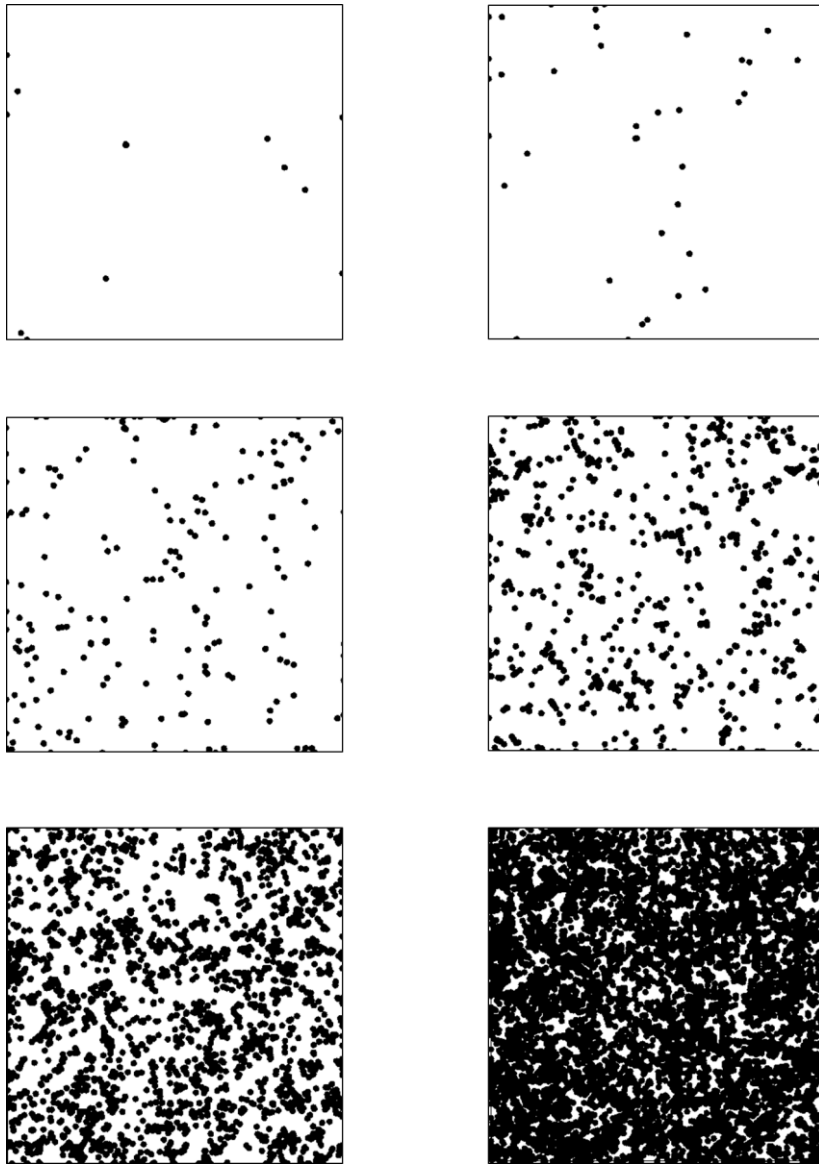
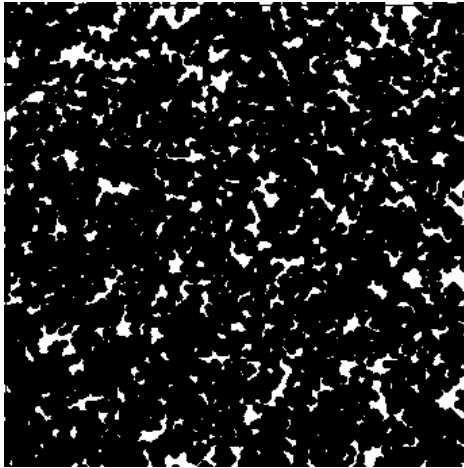


Figure 5-6 A binary plot of extracted intertwining scope based on the number of NWs (100, 200, 500, 1000, 2000, and 4000 EA)



**Figure 5-7 5000 NWs covered 88.9 % of the unit area.**

# Chapter 6

## Laser-Induced Biphasic Metallic Composite

This chapter discusses laser-induced biphasic metallic composite (LIBMC) in both empirical and theoretical ways. Section 6.1 investigates the entanglement phenomenon between LM and metallic NWs empirically through laser parameter study. After that, the theoretical approach is represented to reveal the wettability and the plasmonic effect in section 6.2. Section 6.3 demonstrates and evaluates the stretchable conductor, which has the controlled entanglement degree between LM and metallic NWs. Finally, section 6.4 shows the LIBMC heater as the application.

### 6.1 Entanglement phenomenon

The uniform EGaInPs film is enhanced by the addition of AgNWs, forming the AgNWs-EGaInPs composite. This composite is then deposited onto a stretchable substrate. By using a laser to selectively irradiate the composite, the property of AgNWs-EGaInPs can be controlled. Figure 6-1 shows the changes that occur in the AgNWs-EGaInPs composite as it is exposed to the laser irradiation. When the AgNWs-EGaInPs film is exposed to laser radiation, a rapid photothermal reaction is

induced. This reaction may be aided by the localized surface plasmon resonance that occurs at the interface between the AgNWs and the EGaInPs, resulting in enhanced light absorption and local heating[136, 137]. The surface plasmon resonance leads to the absorption of light and local heating of the film. The sudden and intense local heating causes the oxide shell around the EGaInPs to break. As a result, the EGaInPs spread throughout the AgNWs-EGaInPs film via different mechanisms, including capillary action through the NW backbone and explosive fragmentation within the matrix, as shown in Figure 6-1(ii).

When the EGaInPs in the affected area are fragmented by the laser, they are referred to as F-EGaIn. The F-EGaInPs cover the surface of the AgNWs, including the junctions, creating an entanglement between the discrete EGaInPs and the AgNW network due to capillarity. The result is a mechanically and electrically robust biphasic metallic composite consisting of AgNWs and particulate EGaInPs, as shown in Figure 6-1(iii). Since the laser irradiation process is a direct-writing technique, the local entanglement, which plays a key role in determining the electrical properties of the corresponding spot, can be easily tuned by adjusting the laser parameters. The degree of entanglement between the AgNWs and EGaInPs can be controlled by adjusting the laser power and scanning speed. These two variables determine the scanning energy density ( $\delta$ ) as shown below[138]:

$$\delta \propto \frac{p}{v} \quad 6-1$$

where  $\delta$  is scanning energy density (J/m),  $p$  is the laser power (W), and  $v$  is the laser scanning speed (mm/s). The sintering region excluding the damaged regime can be roughly divided into three categories depending on the scanning energy

density as shown in Figure 6-2.

Figure 6-3 shows the results of laser irradiation on a vacuum filtered AgNW-EGaInP film. The different areas are labeled region (i), region (ii), and region (iii) in order of increasing scanning energy density. The SEM images reveal the sintering characteristics in each region. In region (i), the SEM image shows that laser irradiation has little effect on the AgNWs and EGaInPs. However, as the laser intensity increases, the EGaInPs break into small pieces, referred to as F-EGaInPs, and gradually adhere to the surface of the AgNWs and other EGaInPs[139, 140]. Finally, in region (iii), where the laser intensity is the highest, the AgNWs and EGaInPs exhibit the maximum degree of entanglement, resulting in the formation of a laser-induced biphasic metallic composite (LIBMC) layer, which consists of an Ag NW network surrounded by EGaIn and its oxide layer.

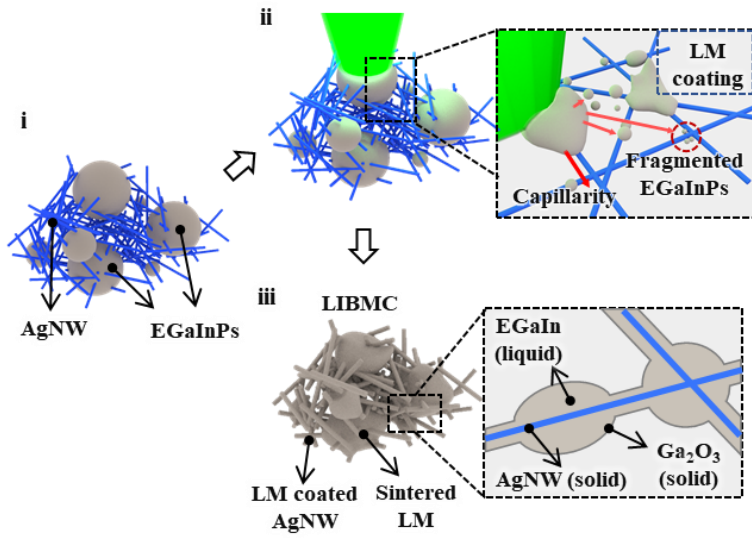


Figure 6-1 Schematic illustration of principle of the LIBMC formation.

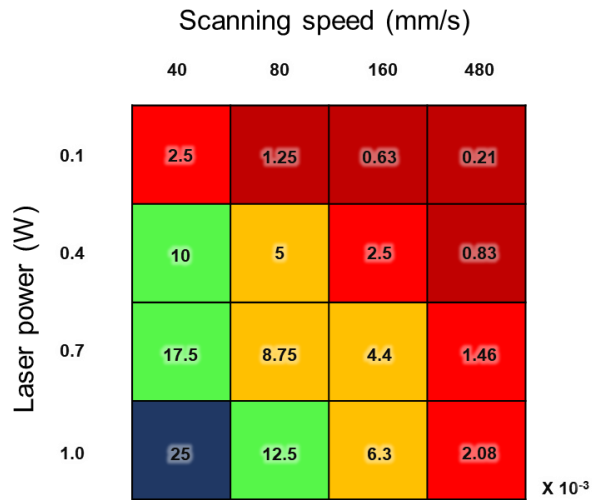
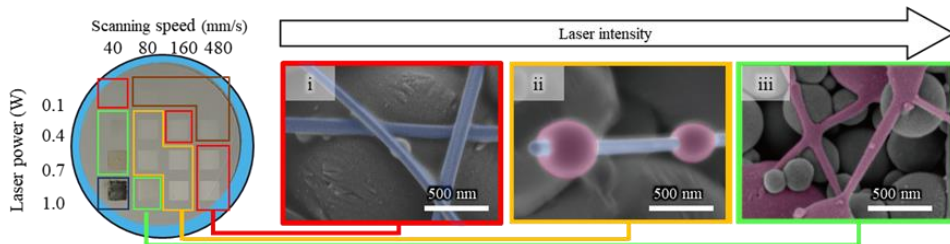


Figure 6-2 Visualization of calculated energy density.



**Figure 6-3** Parametric study results based on the laser power and scanning speed.

## 6.2 Theoretical approach

### 6.2.1 Wettability

AgNW and F-EGaInPs show good wettability despite high surface tension of EGaInPs. The wetting behavior can be described spreading parameter S,

$$S = \gamma_{SV} - (\gamma_{SL} + \gamma_{LV}) \quad 6-2$$

where  $\gamma_{SV}$ ,  $\gamma_{SL}$ ,  $\gamma_{LV}$  are tension between solid-vapor, solid-liquid and liquid-vapor, respectively.

Positive spreading parameter indicates complete wetting whereas negative corresponds to partial wetting. A previous study on sessile nano-droplet on curved surface reported[141].

$$\cos(\theta - \alpha) - \frac{\gamma}{3\gamma_{LV}} \sin(\theta - \alpha) (\cos(\theta) + 1)^2 \left( \frac{\sin(\alpha)(\cos(\alpha) + 2)}{(\cos(\alpha) + 1)^2} - \frac{\sin(\theta) (\cos(\theta) + 2)}{(\cos(\theta) + 1)^2} \right) = \frac{(\gamma_{SV} - \gamma_{SL})}{\gamma_{LV}} + \frac{\kappa \cos(\alpha)}{\gamma_{LV} a} \quad 6-3$$

where  $\theta$  is the contact angle,  $\alpha$  is the roughness parameter of the curvature of solid surfaces,  $\gamma$  is the change in free energy of liquid due to bulk changes in curvature at the boundary due to the Laplace pressure,  $\kappa$  is the line tension, and  $a$  is the radius of the spherical cap as shown in Figure 6-4.

Combining the spreading parameter and the sessile nano-droplet on curve surface relation,

$$S = \gamma_{LV} \left\{ \cos(\theta - \alpha) - \frac{\gamma}{3\gamma_{LV}} \sin(\theta - \alpha) (\cos(\theta) + 1)^2 \left( \frac{\sin(\alpha)(\cos(\alpha) + 2)}{(\cos(\alpha) + 1)^2} - \frac{\sin(\theta) (\cos(\theta) + 2)}{(\cos(\theta) + 1)^2} \right) - 1 \right\} - \frac{\kappa \cos(\alpha)}{a} \quad 6-4$$

From above equation,  $\theta - \alpha$  is the intrinsic contact angle between the tangent of the droplet to the tangent of the surface, and  $\gamma/3\gamma_{LV}$  is the ratio of the surface energies of curvature to deformation and  $\kappa \cos(\alpha)/a$  accounts for the excess line energy at the three-phase interface.

When assuming AgNW as flat plate ( $\alpha = 0$ ) for simplicity,

$$S = \gamma_{LV} \left\{ \cos(\theta) + \frac{\gamma}{3\gamma_{LV}} \sin^2(\theta) (\cos(\theta) + 2) - 1 \right\} - \frac{\kappa}{a} \quad 6-5$$

with neglecting the ratio of the surface energies of curvature to deformation and excess line energy at the three-phase interface,

$$S = \gamma_{LV} (\cos(\theta) - 1) \quad 6-6$$

The above equation is identical to that derived from the Young–Dupré equation. From the experimental measurement of the contact angle[129],

$$0 < \theta < \frac{\pi}{2} \quad 6-7$$

In conclusion,  $S < 0$ , i.e., particulate EGaInPS on the AgNW is partial wetting with high wettability.

### 6.2.2 Plasmonic effect

The entanglement between the AgNWs and EGaInPs is a result of the plasmonic effect. As previously discussed in section 6.1, when the film is exposed to laser radiation, a rapid photothermal reaction is induced as shown in Figure 6-5[142]. The surface plasmon resonance leads to the absorption of light and local heating, which may be aided by the localized surface plasmon resonance that occurs at the interface between the AgNWs and the EGaInPs[143]. This resonance enhances the absorption of light and increases local heating, as reported in previous studies [144, 145].

Entanglement between EGaInPs and AgNWs only occurs through the photothermal effects of laser processing, not in a general high-temperature environment. Figure 6-6 shows the results of exposing thermal energy to an AgNW-EGaInP sample for a sufficient amount of time. The samples were heated in a thermal furnace for 60 minutes at 200 °C and 400 °C, respectively. When the target temperature was 200 °C (Figure 6-6(a)), there was no interaction between the AgNWs and EGaInPs due to insufficient thermal energy, and the two elements could be detected separately in EDS analysis. However, when the target temperature was 400 °C (Figure 6-6(b)), the surface of the EGaInPs was distorted rather than being converted into particulate EGaInPs. Additionally, the AgNWs melted and lost their straight shape due to the extremely high thermal energy. The formation of LIBMC is a unique feature of laser processing.

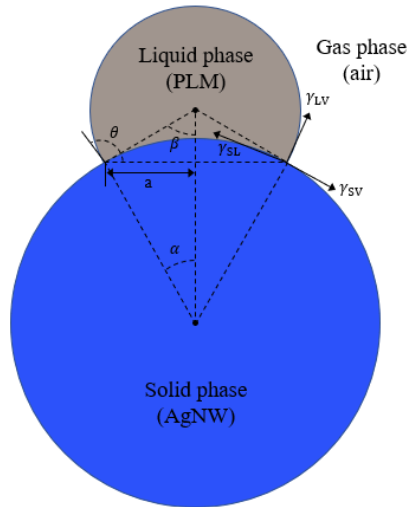


**Figure 6-4 Schematic representation of the AgNW-EGaInPs**

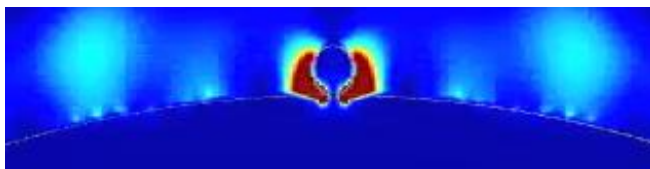


**Figure 6-5 Result of FDTD simulation at AgNW junction**

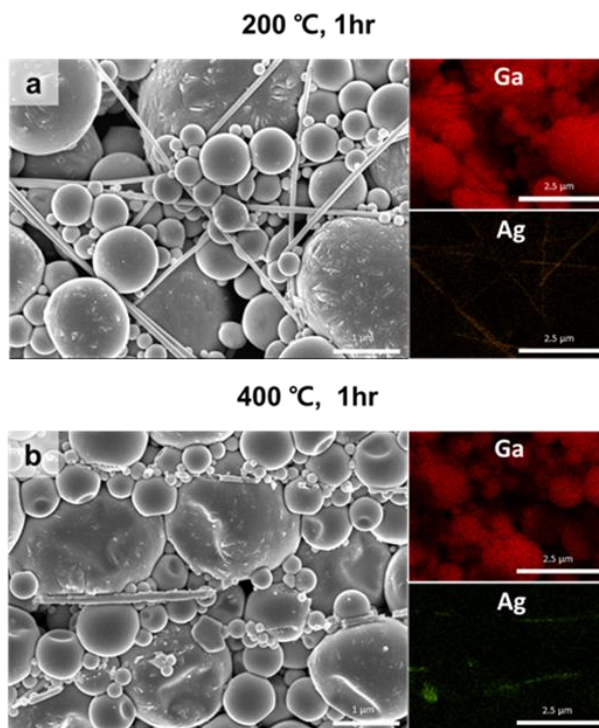


**Figure 6-6** AgNW-EGaInPs film in high temperature environment.

## 6.3 The degree of entanglement between EGaIn and AgNW

### 6.3.1 A quantitative analysis

During the laser process, there are differences in the results between using bulk EGaIn (Figure 6-7) and EGaInPs (Figure 6-8). When laser radiation is applied, the EGaInPs rupture and some of them become F-EGaInPs through splashing. The non-particulate EGaInPs tend to sinter with each other. The formation of LIBMC occurs due to the instant heating. By irradiating the AgNW-EGaInPs film with laser radiation, F-EGaInPs are formed, and the capillary effect helps the EGaInPs adhere to the AgNWs.

Figure 6-9 illustrates the phenomenon in which EGaIn covers the surface of the AgNWs when laser radiation is applied, as observed through energy dispersive X-ray spectroscopy (EDS) analysis. Without laser irradiation conditions (first line), the Ag and Ga elements are clearly distinguishable from each other in the EDS analysis. However, when the laser is irradiated with intermediate intensity conditions, the Ag elements are not detected in the EDS analysis, even though the AgNWs are still visible in the SEM image (red circle). Only the Ga elements are present. In high-intensity laser conditions, the Ga elements are present in a thick, straight line (red circle). Figure 6-10 is an X-ray diffraction (XRD) analysis result, obtained using a D80-Advance instrument from Bruker, indicating that the Ag element is not detected after laser irradiation and only gallium oxide ( $\text{Ga}_2\text{O}_3$ ) is detected on the surface. By comparing this result with a datasheet, it is confirmed that the surface of the LIBMC consists only of  $\text{Ga}_2\text{O}_3$  due to the entanglement effect between the AgNWs and EGaIn, as shown in Figure 6-11.

### 6.3.2 Analysis of etching

The laser irradiation of the AgNWs-EGaInPs film allows for the patterning of electrodes on the stretchable substrate by selectively irradiating certain areas. The oxide layer of EGaIn can be easily removed using a basic solution [49]. The LIBMC conductor can then be separated from the AgNW-EGaInPs film using a simple NaOH solution as an etchant. The etching resistance increases with the laser irradiation intensity due to the entanglement between the AgNWs and EGaInPs, enabling precise patterning of the electrodes on the stretchable substrate.

Figure 6-12 shows the results of the etching process. Region (i), where the laser intensity is weak, has faint or erased patterns, while regions (ii) and (iii) show better patterning capabilities due to the increased entanglement from higher laser intensities. The SEM images show the details after the etching process. Figure 6-12(i) shows that the structure is maintained along the trace of the LIBMC, but in the rest of the region, the remaining EGaInPs that were peeled off from the oxide shell due to the NaOH solution gather and merge to create a bulky EGaIn structure due to the high surface tension of EGaIn. In this process, only the LIBMC remains, and the rest of the film is separated. As the laser intensity increases, the trace of the LIBMC becomes broader and more robust. In region (iii), when the surface of the film is evenly irradiated with a high intensity laser, the structure is well defined without interspatial gaps, and the region below the surface of the film is not affected by the etchant solution. Figure 6-13 shows that the separation of the LIBMC conductor from the AgNW-EGaInPs film is possible for arbitrary patterns through the same etching process. It is important to note that the presence of AgNWs is also critical in

the current etching process. Without AgNWs, the EGaInPs film melts and disappears in the basic solution, even after the laser irradiation process.

Figure 6-14 schematically explains the etching mechanism. When the film composed of AgNWs and EGaInPs is irradiated by a laser, the two substances are sintered and agglomerated to create an entangled structure of AgNWs and particulate EGaInPs. Due to the difference in etching resistance caused by the degree of entanglement, the LIBMC conductor remains intact, while the rest of the film turns into lump debris and floats in the solution. Meanwhile, the bottom surface of the LIBMC conductor, which is directly in contact with the substrate, is attached to the substrate by laser irradiation. Figure 6-15 shows SEM images illustrating the detailed mechanism of adhesion. When a laser is applied to the AgNW-EGaInPs film in contact with the substrate, the EGaInPs lose their spherical shape and become attached to the substrate, forming an anchor[146] (Figure 6-15(i)). The LIBMC layers are then piled on and entangled to the anchor to maintain a vertical stacked structure (Figure 6-15(ii)).

In order to verify the effectiveness of direct circuit patterning, a hand-shaped circuit was fabricated using the selective laser writing and etching process shown in Figure 6-16. The circuit consists of single lines with a minimum interval of 150  $\mu\text{m}$  between them, as shown in the computer-aided drawing in Figure 6-16(i). After the fabrication process, the resulting circuit was inspected and found to be free of defects, as shown in Figure 6-16(ii). Additionally, LIBMC patterns featuring overlapping crosses were also successfully fabricated, as seen in Figure 6-16(iii). Upon inspection of the intersection points using an optical microscope, it was found that the lines were connected without defects and had a width of approximately 25  $\mu\text{m}$ ,

as shown in the inset. The LIBMC conductor was successfully fabricated on various substrates, including PDMS, PET, and PI film, as shown in Figure 6-17. These results demonstrate that the current process is capable of easily creating robust, high-resolution EGaIn-based conductors directly on a wide range of substrates.

Meanwhile, to understand the scalability of LIBMC, it is helpful to review the theoretical contents with laser system illustrated in Figure 6-18. The system consists of a continuous wave (CW) diode-pumped ND: YAG laser (Lighthouse Photonics, Sprout-D) operating at a wavelength of 532 nm, which provides a localized beam source. The laser beam is then passed through a half-wave plate (HWP) and a polarized beam splitter (PBS), which are used to adjust the laser power and polarization. The beam is then directed through the galvano mirror scanner system (Scanlab, HurrySCAN II) and an f-theta telecentric lens (Linos with  $f = 100$  mm) to enable rapid scanning of the focused laser spot on a 2D plane. The resulting laser spot size, under the current optical settings, is estimated to be approximately  $10 \mu\text{m}$  in diameter. As shown in Figure 6-19, the laser light source can take the form of either a Gaussian beam or a flat-top beam. In the experiments conducted in this thesis, a Gaussian beam was used as the light source. The Gaussian beam is a radially symmetrical distribution whose electric field variation is described by the following equation:

$$E = E_s \exp\left(-\frac{r^2}{\omega_0^2}\right) \quad \mathbf{6-8}$$

where  $r$  is defined as the distance from the center of the beam, and  $\omega_0$  is the radius at which the amplitude is  $1/e$  of its value on the axis [147]. The laser intensity has Gaussian distribution from the center of the beam. Considering the properties of

these Gaussian beams, it can be inferred that even if the minimum resolution of the focus is around 10  $\mu\text{m}$ , it is still a valid experimental result that the experimentally obtained minimum line width is approximately 20  $\mu\text{m}$ .

### **6.3.3 Assessment of electromechanical behavior**

This section presents an analysis of the electromechanical behavior of LIBMC. The measurement sample and method are described in detail below. A rectangular patterned line measuring  $2 \times 10$  mm was created for strain testing. To ensure stable resistive contact, a small amount of EGaIn was smoothed between the patterns and copper tape. The device was encapsulated in EcoFlex and supported by VHB (3M) from the back for reliable gauge factor analysis. Despite these precautions, the device was also tested without encapsulation and support in order to prevent interference from emissivity in the IR camera images. The sample was stretched at a velocity of 1 mm/s for gauge factor study and 5 mm/s for 12000 cycle tests using a motorized linear stage (VT-80 with C-663 Mercury Step Controller, Physik Instrumente).

To ensure the accuracy of the measured data, the following points were taken into consideration. At least three LIBMC samples were fabricated for each laser condition. When measuring sheet resistance, the measurement was repeated five times on one sample at different points to obtain statistically reliable data. Resistance measurements with strain were only performed once per sample because the substrate was stretched or broken after measurement due to excessive tensile strength. The measured resistance data, which changes according to strain, was filtered using Origin PRO 2019 software (Origin Lab) to remove noise from the instrument using

the following setup: method: FFT filter, points of window: 10. The relationship between strain and relative change in resistance was only adopted when at least two of the three samples showed the same tendency.

Figure 6-20 shows the sheet resistance of the resulting LIBMC before and after the etching process, which are represented by red and blue colors, respectively. In both etching conditions, the measured sheet resistance is inversely proportional to the laser intensity due to the difference in the degree of entanglement. All LIBMC conductors fabricated with a laser power of 0.5 W were removed from the substrate during the etching process, resulting in a lack of measured data. Overall, the measured sheet resistances are similar for both the before- and after-etching conditions because the conductivity of the final LIBMC is solely determined by the degree of entanglement between the AgNW and EGaInPs. The rest of the LIBMC, which consists of non-irradiated EGaInPs as inherent insulators due to the gallium oxide layer at each surface, remains unaffected.

Figure 6-21 shows the relationship between strain and relative change in resistance according to laser intensity. The relative change in resistance before irradiating the laser is 3.8 at 100 % strain, and this value decreases gradually with an increase in laser intensity. When the laser power is 1.9 W, the relative resistance value is approximately 1.27. The conductivity of each conductor was then calculated using the following formula:

$$\sigma = \frac{l}{Rwt}, \quad 6-9$$

where  $l$  is the sample length,  $R$  is the measured resistance,  $w$  is the sample

width, and  $t$  is the sample thickness. The initial conductivity of the LIBMC conductor ranges from  $1.23 \times 10^4 \text{ Sm}^{-1}$  (no laser) to  $8.65 \times 10^5 \text{ Sm}^{-1}$  (1.9 W of laser power). As previously mentioned, laser irradiation leads to the entanglement of AgNW and EGaInPs, as EGaInPs are converted to F-EGaInPs, which easily stick to surrounding substances including the NW junction, which is most vulnerable to mechanical disturbances. This results in higher conductivity and lower gauge factor. However, the behavior of the gauge factor changes after the etching process, as shown in Figure 6-22. The slopes of all lines in the graph converge to a constant value of approximately 1.27. During the etching process, individual EGaInPs, which are largely responsible for the increase in resistance under strain, disappear, and only the LIBMC remains. As a result, the gauge factor converges to its lowest value. Figure 6-23 shows the repeatability of the LIBMC conductor. The sample consists of a PDMS substrate (PDMS), the LIBMC conductor (with a width of 2 mm and length of 10 mm), and an encapsulation layer (Ecoflex). The experiment was repeated 12000 times with a total operating profile of 2.5 seconds, including 1 second of stretch, 0.25 seconds of rest, 1 second of return, and 0.25 seconds of rest at a speed of 10 mm/s. The repeatability of the LIBMC conductor is consistently maintained for 12000 cycles. In summary, the scheme, which utilizes laser-induced entanglement between AgNW and EGaInPs and is supported by direct patterning capability with superior mechanical stability, produces a stretchable conductor that is relatively insensitive to applied strain up to 100 %.

Finally, the electromechanical behavior of each material was evaluated by making electrodes on gloves, as shown in Figure 6-24. An electrode made of AgNWs was installed on the little finger, and an electrode made of AgNWs and LM was on

the ring finger. The LIBMC electrode treated with a laser was placed on the middle finger. Lastly, an LIBMC electrode extracted from the etching process was on the index finger. The presence of LM showed a significant difference in resistance change compared to the data from the electrodes on the ring and little fingers. Furthermore, the entanglement effect induced by laser irradiation was indirectly verified by comparing the data from the middle and ring fingers. Also, NaOH-treated LIBMC was judged to be more suitable for electrodes than a sensor based on the data from the index and middle fingers.



**Figure 6-7** Laser irradiation to the mixture of bulk EGaIn and AgNWs

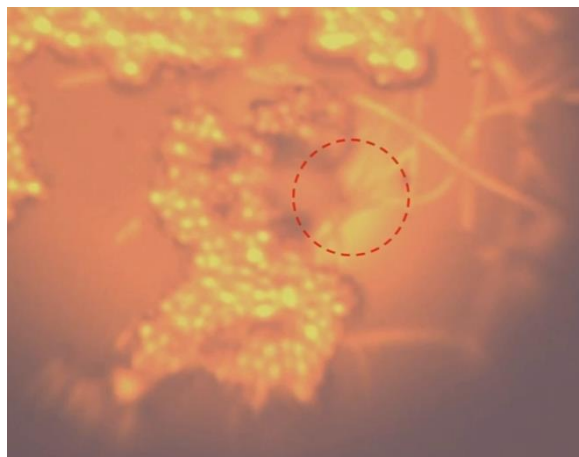


**Figure 6-8** Laser irradiation to the mixture of EGaInPs and AgNWs

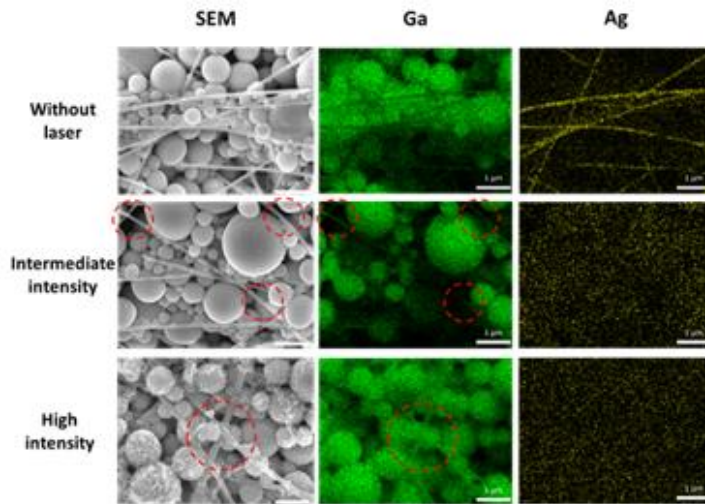


Figure 6-9 SEM and EDS for Ga and Ag components in the LIBMC

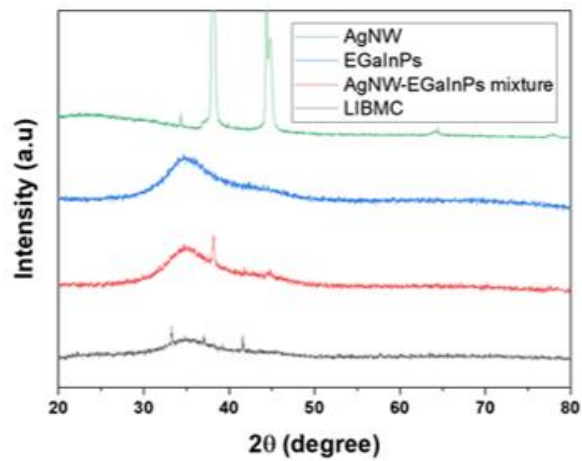


Figure 6-10 Relative comparison of XRD data

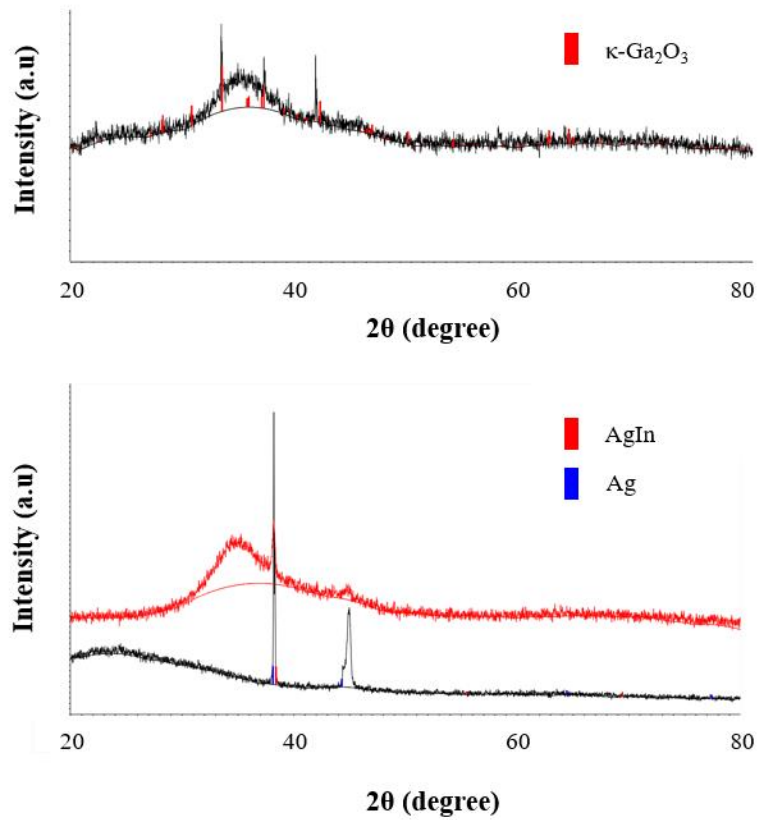


Figure 6-11 XRD results of the LIBMC (top) and AgNW-EGaIn film (bottom)

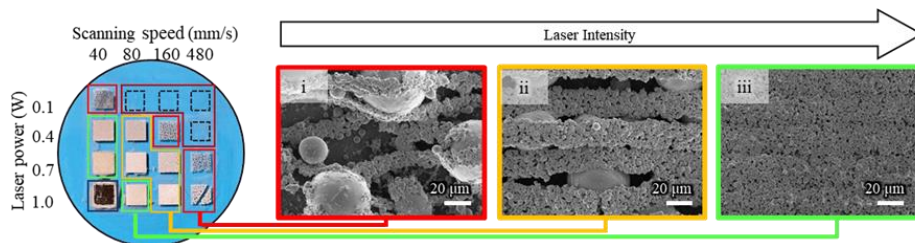


Figure 6-12 Etching result of LIBMC with SEM images based on the laser intensity.

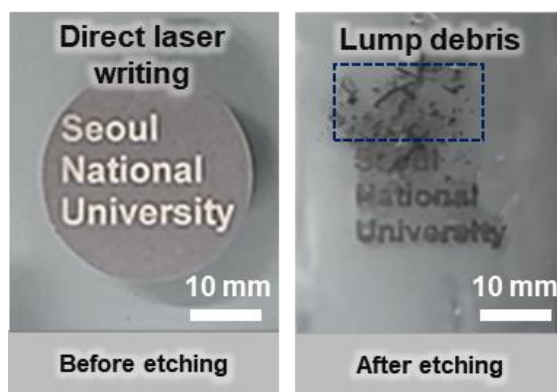


Figure 6-13 LIBMC electrode before and after etching process.

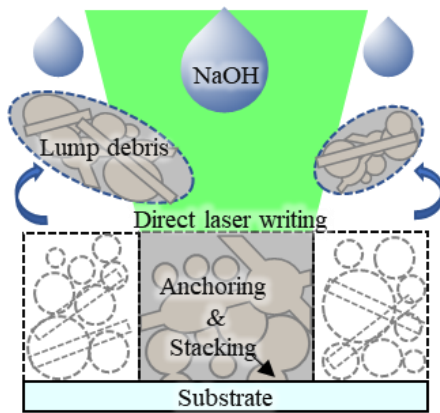


Figure 6-14 Schematic illustration of the selective laser patterning and etching in the AgNWs-EGaInPs film.

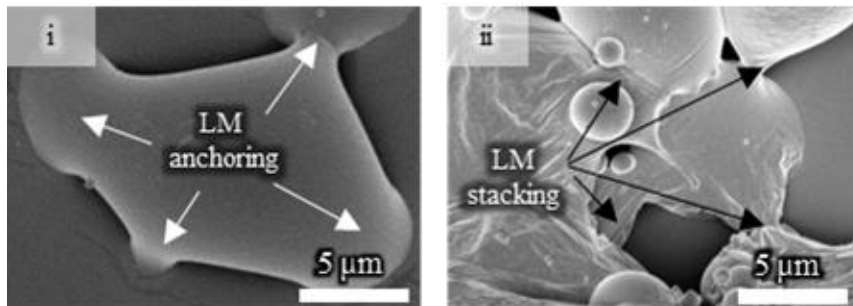


Figure 6-15 SEM images for (i) the LM anchoring and (ii) the LM stacking

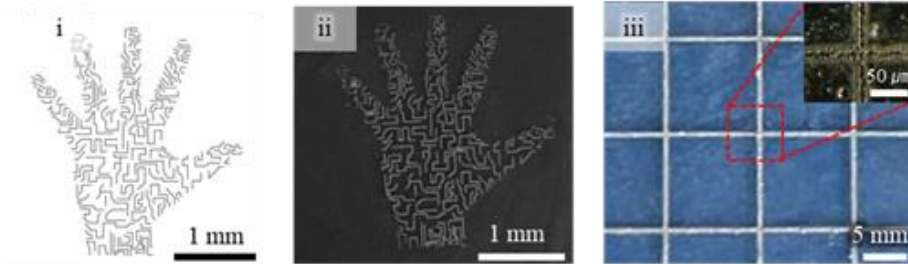


Figure 6-16 LIBMC conductor: (i) computer-aided drawing, (ii) prototype, and (iii) grid.

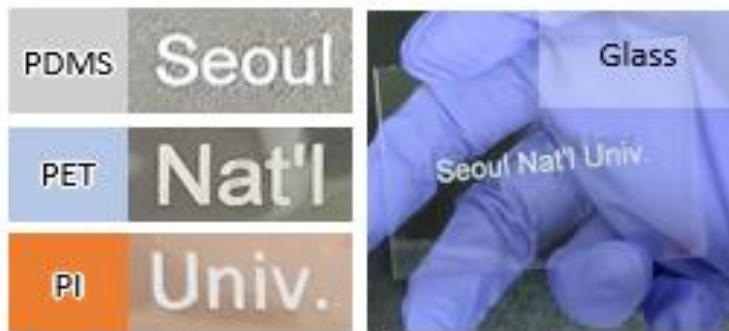


Figure 6-17 Direct laser patterning on various substrates.

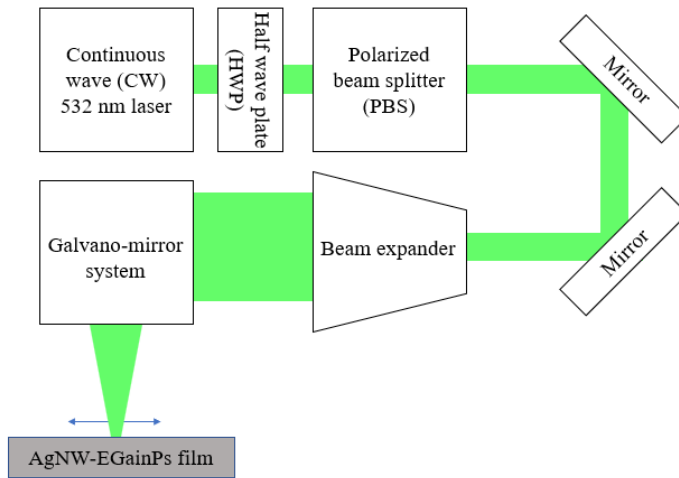


Figure 6-18 Schematic illustration of the laser system

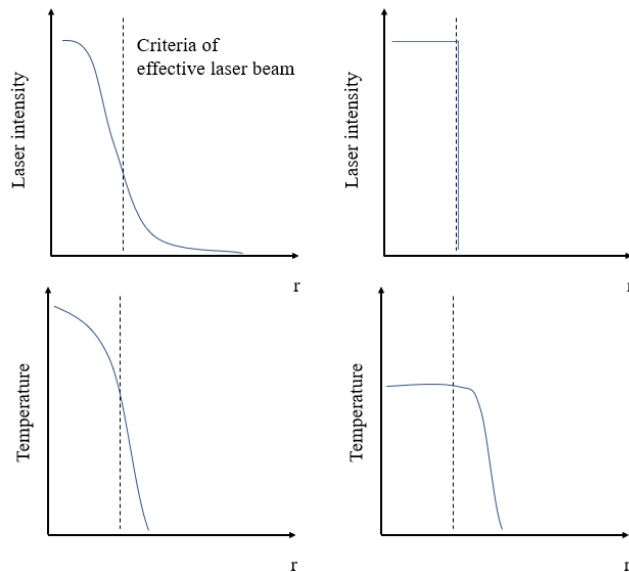
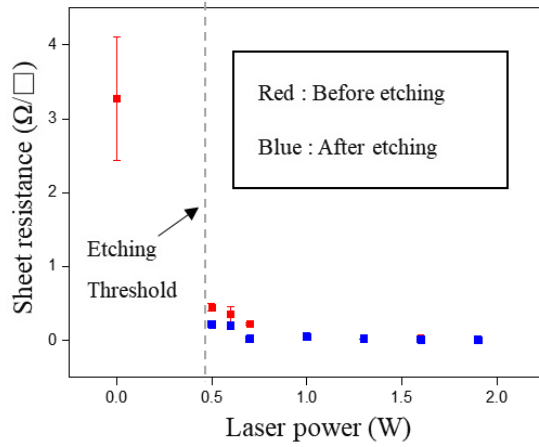
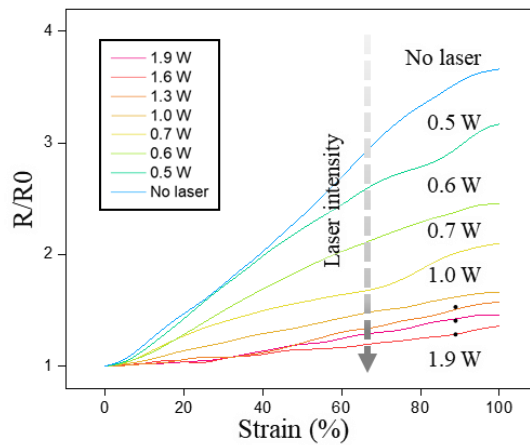


Figure 6-19 Characteristic profile for Gaussian (left) and flat-top beam (right)



**Figure 6-20** Sheet resistance measurement as a function of laser power before (red) and after (blue) etching.



**Figure 6-21** Relative change in resistance as a function of uniaxial tensile strain on PDMS before etching with various laser conditions.

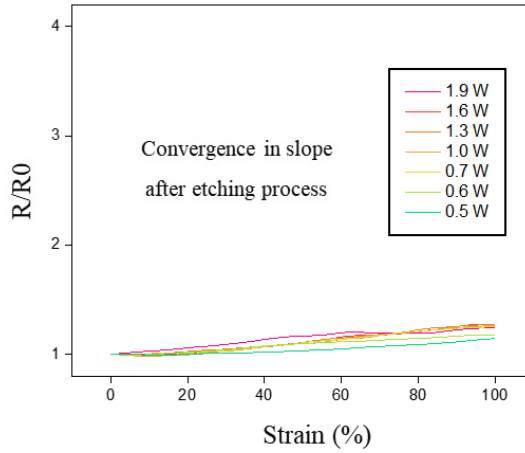


**Figure 6-22** Relative change in resistance as a function of uniaxial tensile strain on PDMS after etching with various laser conditions.

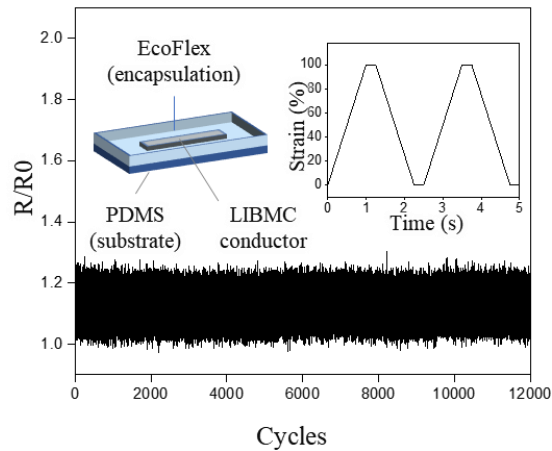


**Figure 6-23** Cyclic test data for the LIBMC conductor.

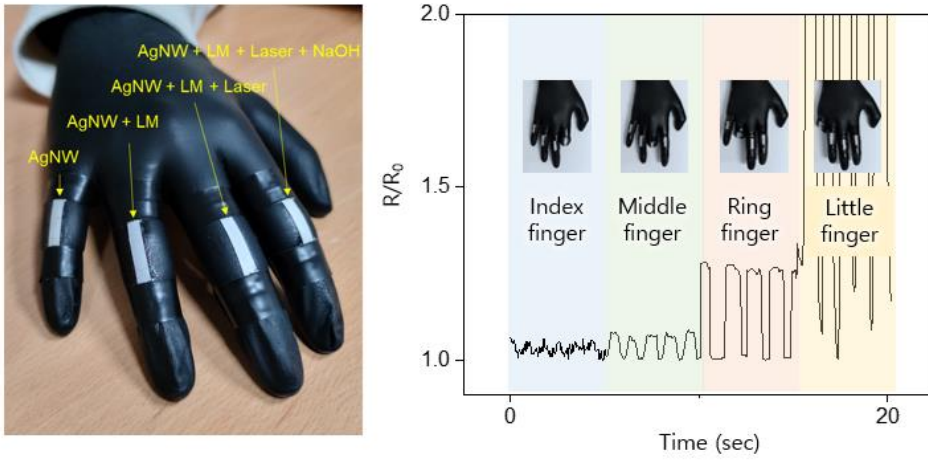


**Figure 6-24 Performance assessment by types of the stretchable electrode**

## **6.4 Utilization of LIBMC**

### **6.4.1 Necessity of the LIBMC heater**

This section explores the usage for LIBMC by examining its potential applications. A heater is a device that imparts or holds heat. Among the various types of heaters, electric heaters are widely used industrially due to their ease of control based on Joule's law. In the semiconductor manufacturing process, a heater is often used in the photolithography process to dry photoresist applied to a wafer. As shown in Figure 6-25, it is important to control the temperature of the heater by region to ensure uniform drying of the photoresist. To achieve this, each region of the heater is divided and controlled by individual electrical controllers based on Joule's law. However, the use of multiple controllers can introduce side effects, such as hardware issues caused by the large number of wires connecting the controllers to the heater, and spatial constraints in the facility from the deployment of numerous controllers. Figure 6-26 illustrates this process. Each region of the heater is divided for sophisticated temperature control, and different electrical controllers regulate each region based on Joule's law. However, as the number of controllers increases, side effects also increase. Not only is there a hardware problem caused by numerous wires connecting the controller to the heater, but there are also spatial constraints in the facility to deploy many controllers.

The proposed LIBMC offers a solution to the limitations of traditional heating wires, providing several advantages. Firstly, LIBMC is able to adjust the resistance of a heating wire more freely than traditional heating wires, which are limited in their resistance range due to the intrinsic properties of their materials. LIBMC, on the other hand, is not constrained by external spatial limitations and can change its own

electrical conductivity. Secondly, the monolithic nature of LIBMC allows for the design of resistance in any desired area, enabling the temperature of multiple regions to be modified independently using only a single electrode. Thirdly, the ability to control temperature using a single resistance line allows for a drastic decrease in the number of electric controllers needed. Previously, controllers had to be used in proportion to the number of controlled areas, but LIBMC no longer requires a controller for each zone, leading to fewer connection points between the heater and controllers and increased convenience in terms of space utilization and facility maintenance.

#### **6.4.2 Demonstration of prototype**

The goal of this section is to fabricate a prototype of a monolithic LIBMC heater with programmable conductivity and strain-invariant gauge factor under 50% strain conditions, using the knowledge and techniques developed throughout the dissertation. The conceptual image of the LIBMC heater is shown in Figure 6-27. The process involves transferring a uniform thickness of AgNW-EGaInPs film to stretchable substrates and using laser engraving to create patterns that can serve as both heating wire and electrode monolithically. The laser intensity is carefully controlled to enable this process.

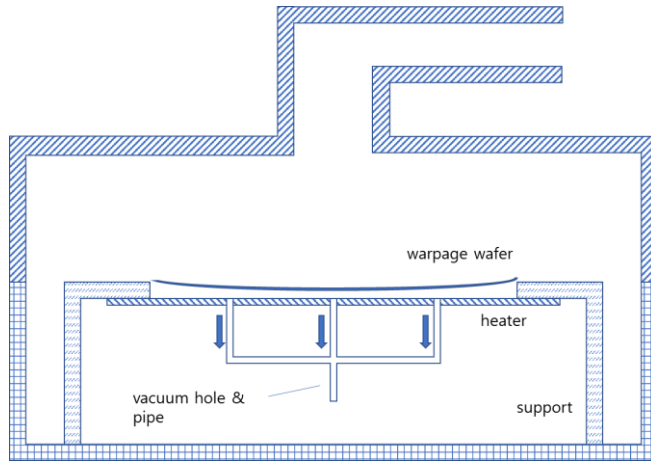
As illustrated in Figure 6-28, the LIBMC heater is designed by dividing the region into four types based on the laser power used. In region (a), the lowest laser power (0.5 W) is applied to create a high resistance within the available processing window. Regions (b) and (c) are designed to achieve lower resistance values

monolithically using higher laser powers (0.6 W and 0.7 W, respectively). Region (d) is designed to serve as a LIBMC conductor for wiring purposes and therefore requires a high laser power (1.6 W) to minimize heat generation in that area. The prototype of the LIBMC heater is fabricated monolithically according to this design, as shown in the white dotted boxes, using different laser powers to create spatially-varying LIBMC conductors that serve as both heating wire and electrode simultaneously.

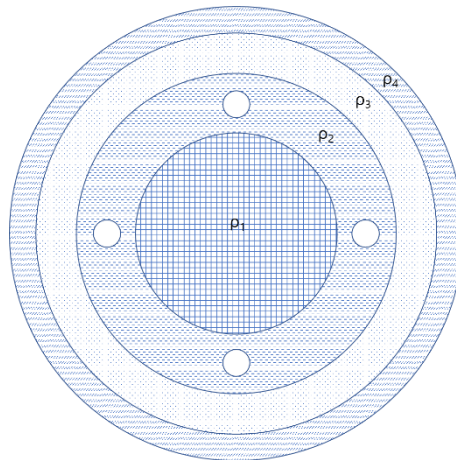
In Figure 6-29, a voltage is applied to the fabricated LIBMC heater to measure the average temperature of each region. The LIBMC heater data was captured and displayed using an IR camera (A645sc, FLIR) while applying a DC voltage to the heater via a DC power supply (K6003D, ICAN). Despite being made of the same materials, the temperature of each region increases to different extents due to the variation in conductivity caused by the laser power regulation. At 50 seconds, the temperature of region (d) is lower than that of regions (a) and (b). This result suggests that the thermal properties of the LIBMC heater are determined by the programmed resistance characteristics of each region rather than by heat transfer through thermal conduction. The infrared camera image taken every 10 seconds shows the monolithically fabricated LIBMC heater area, outlined in white dotted lines. The temperature increases according to the resistance characteristics of each region, with the parts used as electrodes exhibiting relatively low heat generation.

Figure 6-30 shows the stretchability performance of the LIBMC heater when operating under tensile conditions. The test was conducted after applying a voltage of 4 V for 3 minutes to fully saturate the temperature. As the strain increases up to 50%, the average temperature of each region remains unchanged, demonstrating the

stretchability of the monolithically fabricated LIBMC conductor. The infrared camera image shows that the temperature distribution on the heater is maintained while the heater is stretched up to 50% under uniaxial tensile conditions.



**Figure 6-25** Example of industrial application as electric heater



**Figure 6-26** Differences of heating wire resistivity by zone

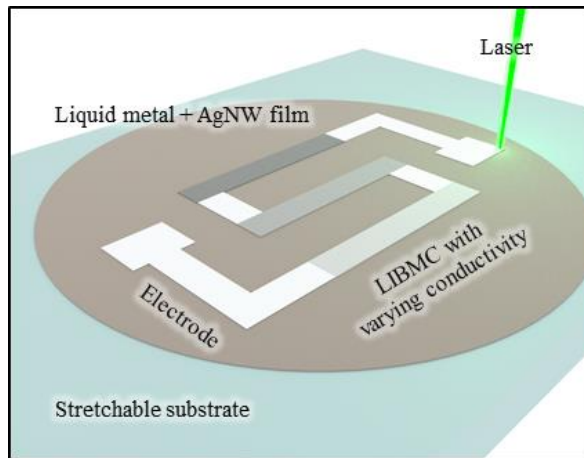


Figure 6-27 Conceptual image of LIBMC heater by applying varying conductivity characteristics

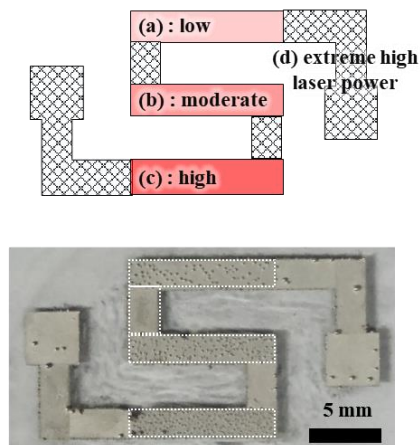


Figure 6-28 LIBMC heater design and fabricated prototype

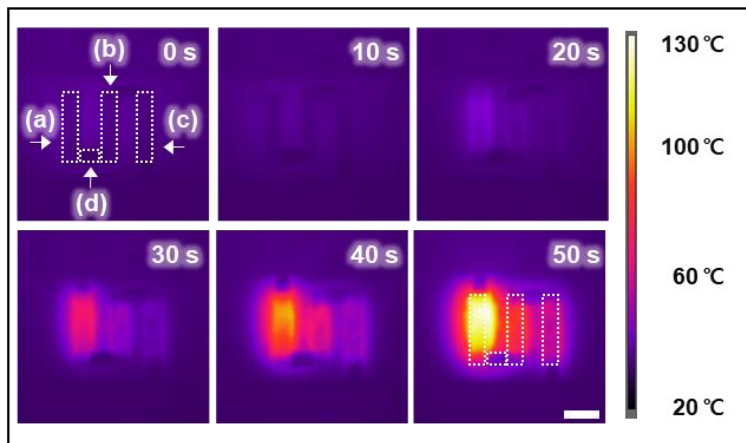
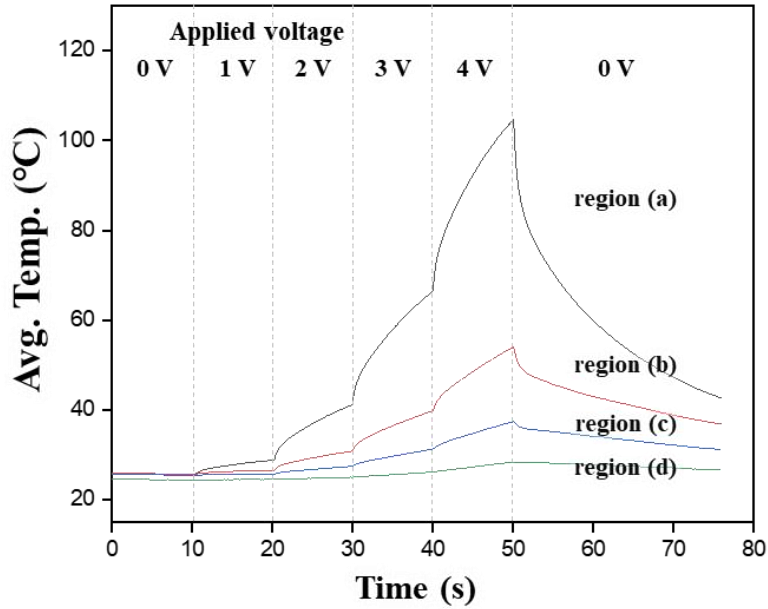
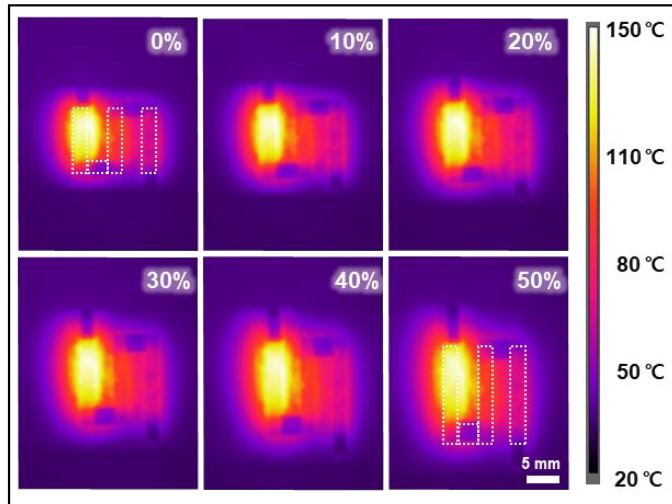
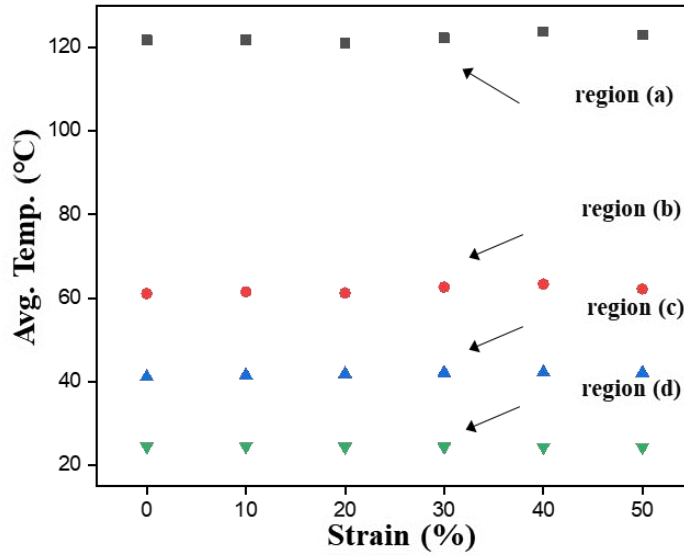


Figure 6-29 Transient average temperature evolution of the LIBMC heater under zero strain at stepwise voltage rise from 0 to 4 V



**Figure 6-30** Average temperature for the regions at a constant applied voltage of 4 V under strain variation

---

---

Sections of this chapter have been published as the following journal article:

**Cho, C.**, Shin, W., Kim, M., Bang, J., Won, P., Hong, S., and Ko, S. H.  
*Monolithically Programmed Stretchable Conductor by Laser-Induced  
Entanglement of Liquid Metal and Metallic NW Backbone*, 2022, *Small*,  
**18**(37), 2202841.

---

---

# Chapter 7

## Conclusions

### 7.1 Contributions and significance

This dissertation presents a laser-based design framework for LM and metallic NWs, including an analysis of metal alloys. While there have been many individual studies on LM, metallic NWs, and lasers, there has been little research on the fusion of these three fields. The dissertation fills this gap by providing a comprehensive overview of the potential applications of this fusion, from the basics to practical applications. It lays the foundation for future research in this area. The core contents of the dissertation are summarized in Figure 7-1, which shows the use of EGaInP as a 0D structure and AgNW as a 1D structure, which are then subjected to laser irradiation to adjust their properties. As shown in the figure, the degree of entanglement between the two materials changes according to the intensity of the laser. In the upper left of the figure, where the laser is strongly applied, the LM completely covers the AgNWs. On the other hand, in the bottom right of the figure, there is no interaction between LM and AgNWs without laser treatment. In the center part of the figure, the silver NWs are partially covered with EGaIn. These differences in the degree of entanglement lead to varying conductivity and ease of patterning.

One of the key contributions of this dissertation is the development of an easy

patterning process. In previous studies, LM patterns have been fabricated using complex and costly fab processes that also progressed in toxic environment. In contrast, the dissertation presents a simple and straightforward patterning process that can be carried out at room temperature. This broadens the potential for wider use of this approach in future studies. Another significant aspect of this dissertation is the discovery of controllable, varying conductivity, which has the potential to unlock new applications in the future. Traditionally, materials have had fixed conductivity due to their intrinsic properties, limiting their usefulness. By enabling the control of conductivity, however, this dissertation opens the door for creative uses such as the monolithic fabrication of heating wire and electrode. Furthermore, it is essential to perform a new simulation study that incorporates a mixture of 0D and 1D structures. This simulation can be based on the principles of percolation theory and can provide valuable insights into the interplay between the two dimensionalities. By comparing the results of experiments with those obtained from simulations, it will be possible to make predictions about the optimal experimental conditions even if the initial conditions of the nanowires change in the future. This verification and validation approach will ensure the reliability of the simulation results and help to establish a more comprehensive understanding of the system under study.

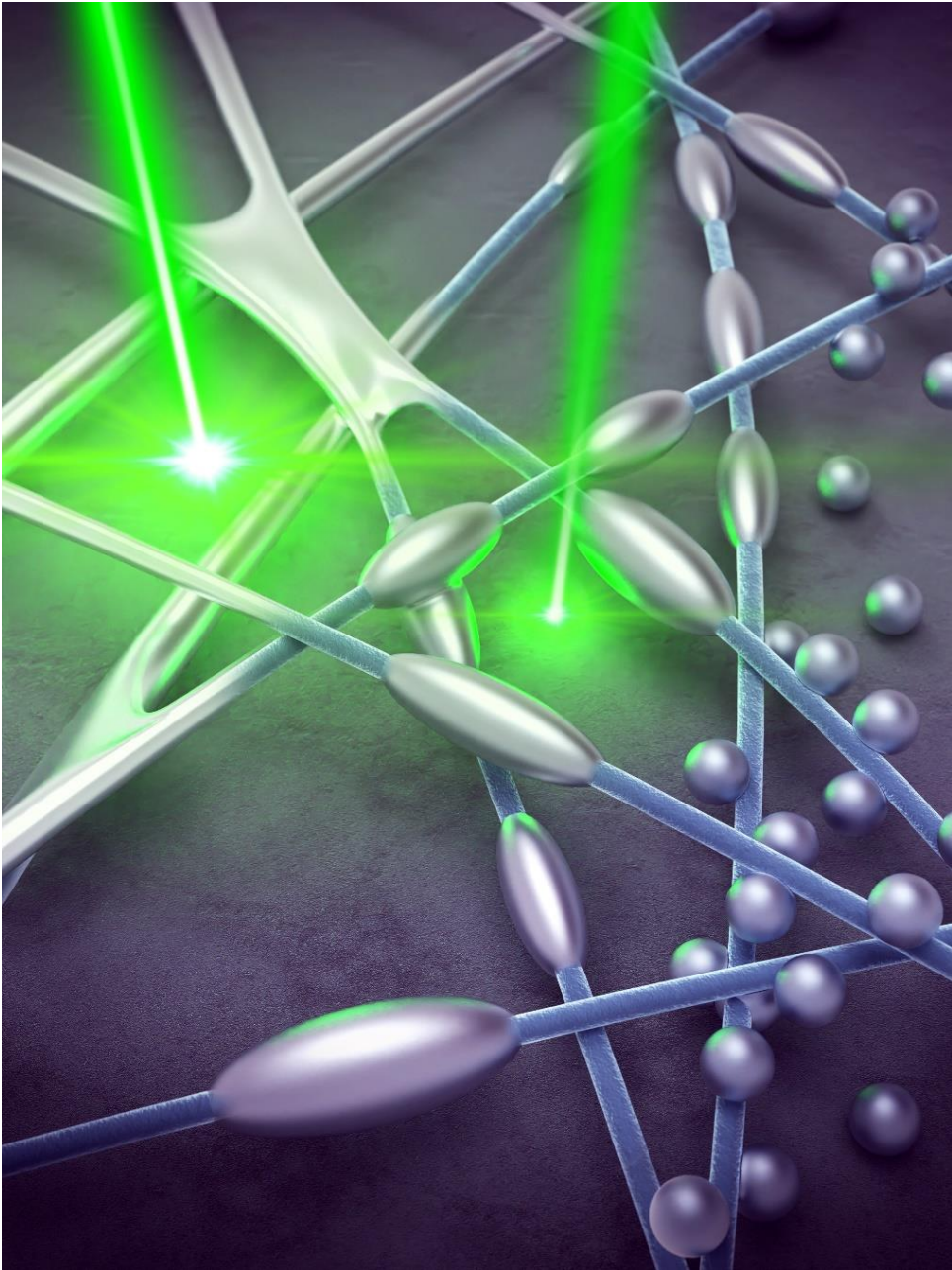


**Figure 7-1 Schematic illustration of crucial points of the LIBMC conductor**

## 7.2 Suggestions for future research

This doctoral dissertation makes a substantial contribution to the field of stretchable electrodes through the utilization of LM, metallic NWs and lasers. While this study has yielded new discoveries through extensive research, there are still areas for improvement. Further investigation and analysis of the strengths and weaknesses of this study can lead to additional breakthroughs in the future.

First, the study includes an innovative approach to simulating NWs, which serves as a reference for future comparisons with synthesized NWs that may exhibit variations in length, thickness, and curvature. This simulation method allows for a more accurate prediction of the NW-LM film properties and its potential applications, especially in the field of stretchable electronics.

Second, the study also demonstrates the improvement of the mechanical properties of the film with increasing amounts of AgNWs, leading to a solid film structure with trapped metal. This could result in a novel method of extracting a free-standing patch using a laser, offering the potential for easy attachment and removal of the film from desired objects[148]. The study sheds light on the current use of CW laser patterning for LM films and the possibility of utilizing UV laser characteristics for cutting as a more efficient method in the future.

Third, this doctoral study also explores the concept of material synergy by mixing different materials in the development of stretchable electrodes. It highlights the potential for finding new and innovative effects by continuing research with other materials, such as bio-friendly electrodes using PEDOT:PSS[149] and the

interrelationship between EGaIn and PSS[150]. The study identifies the potential for creating a bio-friendly electrode with improved conductivity through the combination of LM and pedot:pss, presenting a promising area for future research. By finding the synergy effect of materials, this study opens up new avenues for investigating the potential benefits and applications of combining different materials in stretchable electrodes.

Finally, the study also demonstrates the potential of using LIBMC as a heater, but acknowledges the need for further research and development to meet the demands of industrial applications. This requires a comprehensive evaluation of materials and processes to achieve the desired level of temperature control and high manufacturing yield.

## References

1. Li, G., et al., *Self-powered soft robot in the Mariana Trench*. Nature, 2021. **591**(7848): p. 66-71.
2. Green, J.J. and J.H. Elisseeff, *Mimicking biological functionality with polymers for biomedical applications*. Nature, 2016. **540**(7633): p. 386-394.
3. Xu, C., et al., *High-resolution patterning of liquid metal on hydrogel for flexible, stretchable, and self-healing electronics*. Advanced Electronic Materials, 2020. **6**(1): p. 1900721.
4. Kim, D.-H., et al., *Epidermal electronics*. science, 2011. **333**(6044): p. 838-843.
5. Lin, F., et al., *Soft gold nanowire sponges for strain-insensitive conductors, wearable energy storage and catalytic converters*. Journal of Materials Chemistry C, 2021. **9**(42): p. 15329-15336.
6. Lee, P., et al., *Highly stretchable and highly conductive metal electrode by very long metal nanowire percolation network*. Advanced materials, 2012. **24**(25): p. 3326-3332.
7. Gong, S., et al., *A gold nanowire-integrated soft wearable system for dynamic continuous non-invasive cardiac monitoring*. Biosensors and Bioelectronics, 2022. **205**: p. 114072.
8. Jung, D., et al., *Highly conductive and elastic nanomembrane for skin electronics*. Science, 2021. **373**(6558): p. 1022-1026.
9. Hirsch, A., et al., *Intrinsically stretchable biphasic (solid–liquid) thin metal films*. Advanced Materials, 2016. **28**(22): p. 4507-4512.
10. Dickey, M.D., et al., *Eutectic Gallium-Indium (EGaIn): A Liquid Metal Alloy for the Formation of Stable Structures in Microchannels at Room Temperature*. Advanced

- Functional Materials, 2008. **18**(7): p. 1097-1104.
11. Liu, S., D.S. Shah, and R. Kramer-Bottiglio, *Highly stretchable multilayer electronic circuits using biphasic gallium-indium*. Nat Mater, 2021. **20**(6): p. 851-858.
  12. Ma, Z., et al., *Permeable superelastic liquid-metal fibre mat enables biocompatible and monolithic stretchable electronics*. Nat Mater, 2021. **20**(6): p. 859-868.
  13. Chen, B., et al., *Flexible thermoelectric generators with inkjet-printed bismuth telluride nanowires and liquid metal contacts*. Nanoscale, 2019. **11**(12): p. 5222-5230.
  14. Wang, J., et al., *Printable superelastic conductors with extreme stretchability and robust cycling endurance enabled by liquid-metal particles*. Advanced Materials, 2018. **30**(16): p. 1706157.
  15. Tavakoli, M., et al., *EGaIn-Assisted Room-Temperature Sintering of Silver Nanoparticles for Stretchable, Inkjet-Printed, Thin-Film Electronics*. Adv Mater, 2018: p. e1801852.
  16. Guo, R., et al., *Ni-GaIn Amalgams Enabled Rapid and Customizable Fabrication of Wearable and Wireless Healthcare Electronics*. Advanced Engineering Materials, 2018. **20**(10).
  17. Lee, G., et al., *Omnidirectionally and Highly Stretchable Conductive Electrodes Based on Noncoplanar Zigzag Mesh Silver Nanowire Arrays*. Advanced Electronic Materials, 2016. **2**(8).
  18. Niu, J., et al., *Electrical conductivity change induced by porosity within polymer-derived SiCN ceramics*. Journal of Alloys and Compounds, 2019. **777**: p. 1010-1016.
  19. Hong, S., et al., *Digital selective laser methods for nanomaterials: From synthesis to processing*. Nano Today, 2016. **11**(5): p. 547-564.

20. Kalantar-Zadeh, K., et al., *Emergence of liquid metals in nanotechnology*. ACS nano, 2019. **13**(7): p. 7388-7395.
21. Dickey, M.D., et al., *Eutectic gallium-indium (EGaIn): a liquid metal alloy for the formation of stable structures in microchannels at room temperature*. Advanced functional materials, 2008. **18**(7): p. 1097-1104.
22. Suarez, F., et al., *Flexible thermoelectric generator using bulk legs and liquid metal interconnects for wearable electronics*. Applied energy, 2017. **202**: p. 736-745.
23. Zhu, C., et al., *Stretchable temperature-sensing circuits with strain suppression based on carbon nanotube transistors*. Nature Electronics, 2018. **1**(3): p. 183-190.
24. Shu, J., et al., *A liquid metal artificial muscle*. Advanced Materials, 2021. **33**(43): p. 2103062.
25. Park, Y.-L., B.-R. Chen, and R.J. Wood, *Design and fabrication of soft artificial skin using embedded microchannels and liquid conductors*. IEEE Sensors journal, 2012. **12**(8): p. 2711-2718.
26. Vallem, V., et al., *A Soft Variable-Area Electrical-Double-Layer Energy Harvester*. Advanced Materials, 2021. **33**(43): p. 2103142.
27. Wang, S., et al., *A liquid metal-based triboelectric nanogenerator as stretchable electronics for safeguarding and self-powered mechanosensing*. Nano Energy, 2018. **53**: p. 863-870.
28. Won, P., et al., *Recent advances in liquid-metal-based wearable electronics and materials*. Iscience, 2021. **24**(7): p. 102698.
29. Tang, S.-Y., et al., *Gallium liquid metal: the Devil's elixir*. Annual Review of Materials Research, 2021. **51**: p. 381-408.
30. Cheng, S. and Z. Wu, *Microfluidic electronics*. Lab on a Chip, 2012. **12**(16): p. 2782-2791.

31. Hao, X.P., et al., *Self-Shaping Soft Electronics Based on Patterned Hydrogel with Stencil-Printed Liquid Metal*. *Advanced Functional Materials*, 2021. **31**(47): p. 2105481.
32. Park, J.E., et al., *Autonomous Surface Reconciliation of a Liquid-Metal Conductor Micropatterned on a Deformable Hydrogel*. *Advanced Materials*, 2020. **32**(37): p. 2002178.
33. Guo, R., et al., *Cu-EGaIn enabled stretchable e-skin for interactive electronics and CT assistant localization*. *Materials Horizons*, 2020. **7**(7): p. 1845-1853.
34. Neumann, T.V. and M.D. Dickey, *Liquid metal direct write and 3D printing: a review*. *Advanced Materials Technologies*, 2020. **5**(9): p. 2000070.
35. Kong, W., et al., *Oxide-mediated mechanisms of gallium foam generation and stabilization during shear mixing in air*. *Soft Matter*, 2020. **16**(25): p. 5801-5805.
36. Park, Y.-G., et al., *High-resolution, reconfigurable printing of liquid metals with three-dimensional structures*. *Science advances*, 2019. **5**(6): p. eaaw2844.
37. Pan, C., et al., *Visually imperceptible liquid-metal circuits for transparent, stretchable electronics with direct laser writing*. *Advanced Materials*, 2018. **30**(12): p. 1706937.
38. Dejace, L., et al., *Microscale Liquid Metal Conductors for Stretchable and Transparent Electronics*. *Advanced Materials Technologies*, 2021. **6**(11): p. 2100690.
39. Park, Y., et al., *Liquid-metal micro-networks with strain-induced conductivity for soft electronics and robotic skin*. *npj Flexible Electronics*, 2022. **6**(1): p. 1-10.
40. Kim, M.-g., D.K. Brown, and O. Brand, *Nanofabrication for all-soft and high-density electronic devices based on liquid metal*. *Nature communications*, 2020. **11**(1): p. 1-11.

41. Krisnadi, F., et al., *Directed Assembly of Liquid Metal–Elastomer Conductors for Stretchable and Self-Healing Electronics*. *Advanced Materials*, 2020. **32**(30): p. 2001642.
42. Shay, T., O.D. Velev, and M.D. Dickey, *Soft electrodes combining hydrogel and liquid metal*. *Soft Matter*, 2018. **14**(17): p. 3296-3303.
43. Chang, H., et al., *Recoverable liquid metal paste with reversible rheological characteristic for electronics printing*. *ACS applied materials & interfaces*, 2020. **12**(12): p. 14125-14135.
44. Yuan, B., X. Sun, and J. Liu, *Al-NaOH-Composited Liquid Metal: A Fast-Response Water-Triggered Material with Thermal and Pneumatic Properties*. *Engineering*, 2020. **6**(12): p. 1454-1462.
45. Tang, J., et al., *Gallium-based liquid metal amalgams: transitional-state metallic mixtures (TransM2ixes) with enhanced and tunable electrical, thermal, and mechanical properties*. *ACS applied materials & interfaces*, 2017. **9**(41): p. 35977-35987.
46. Liu, S., D.S. Shah, and R. Kramer-Bottiglio, *Highly stretchable multilayer electronic circuits using biphasic gallium-indium*. *Nature Materials*, 2021. **20**(6): p. 851-858.
47. Yun, I., et al., *Transferable transparent electrodes of liquid metals for bifacial perovskite solar cells and heaters*. *Nano Energy*, 2022. **93**: p. 106857.
48. Kim, M.-g., et al., *All-soft supercapacitors based on liquid metal electrodes with integrated functionalized carbon nanotubes*. *ACS nano*, 2020. **14**(5): p. 5659-5667.
49. Ozutemiz, K.B., et al., *EGaIn–metal interfacing for liquid metal circuitry and microelectronics integration*. *Advanced Materials Interfaces*, 2018. **5**(10): p. 1701596.

50. Ma, Z., et al., *Permeable superelastic liquid-metal fibre mat enables biocompatible and monolithic stretchable electronics*. Nature Materials, 2021. **20**(6): p. 859-868.
51. Lee, J., et al., *Recent advances in 1D stretchable electrodes and devices for textile and wearable electronics: materials, fabrications, and applications*. Advanced Materials, 2020. **32**(5): p. 1902532.
52. Liu, H., et al., *Liquid metal gradient fibers with reversible thermal programmability*. Materials Horizons, 2020. **7**(8): p. 2141-2149.
53. Chen, G., et al., *Superelastic EGaIn composite fibers sustaining 500% tensile strain with superior electrical conductivity for wearable electronics*. ACS applied materials & interfaces, 2020. **12**(5): p. 6112-6118.
54. Wang, Q., Y. Yu, and J. Liu, *Preparations, characteristics and applications of the functional liquid metal materials*. Advanced Engineering Materials, 2018. **20**(5): p. 1700781.
55. Lin, Y., J. Genzer, and M.D. Dickey, *Attributes, Fabrication, and Applications of Gallium-Based Liquid Metal Particles*. Advanced Science, 2020. **7**(12): p. 2000192.
56. Zhang, M., et al., *Transformable soft liquid metal micro/nanomaterials*. Materials Science and Engineering: R: Reports, 2019. **138**: p. 1-35.
57. Lin, Y., et al., *Handwritten, soft circuit boards and antennas using liquid metal nanoparticles*. Small, 2015. **11**(48): p. 6397-6403.
58. Lee, G.H., et al., *A Personalized Electronic Tattoo for Healthcare Realized by On-the-Spot Assembly of an Intrinsically Conductive and Durable Liquid-Metal Composite*. Advanced Materials, 2022. **34**(32): p. 2204159.
59. Tang, J., et al., *Unique surface patterns emerging during solidification of liquid metal alloys*. Nature Nanotechnology, 2021. **16**(4): p. 431-439.
60. Morris, N.J., Z.J. Farrell, and C.E. Tabor, *Chemically modifying the mechanical*

- properties of core-shell liquid metal nanoparticles*. *Nanoscale*, 2019. **11**(37): p. 17308-17318.
61. Hafiz, S.S., et al., *Surfaces and interfaces of liquid metal core-shell nanoparticles under the microscope*. *Particle & particle systems characterization*, 2020. **37**(5): p. 1900469.
62. Ma, J., et al., *Liquid metal nanoparticles as initiators for radical polymerization of vinyl monomers*. *ACS Macro Letters*, 2019. **8**(11): p. 1522-1527.
63. Yan, J., et al., *Solution processable liquid metal nanodroplets by surface-initiated atom transfer radical polymerization*. *Nature nanotechnology*, 2019. **14**(7): p. 684-690.
64. Cutinho, J., et al., *Autonomous thermal-oxidative composition inversion and texture tuning of liquid metal surfaces*. *ACS nano*, 2018. **12**(5): p. 4744-4753.
65. Tavakoli, M., et al., *EGaIn-Assisted Room-Temperature Sintering of Silver Nanoparticles for Stretchable, Inkjet-Printed, Thin-Film Electronics*. *Advanced Materials*, 2018. **30**(29): p. 1801852.
66. Li, X., et al., *Evaporation-induced sintering of liquid metal droplets with biological nanofibrils for flexible conductivity and responsive actuation*. *Nature communications*, 2019. **10**(1): p. 1-9.
67. Malakooti, M.H., et al., *Liquid metal nanocomposites*. *Nanoscale Advances*, 2020. **2**(7): p. 2668-2677.
68. Ochirkhuyag, N., et al., *Liquid metal-based nanocomposite materials: fabrication technology and applications*. *Nanoscale*, 2021. **13**(4): p. 2113-2135.
69. Neumann, T.V., et al., *Direct write printing of a self-encapsulating liquid metal-silicone composite*. *Soft Matter*, 2020. **16**(28): p. 6608-6618.
70. Zadan, M., M.H. Malakooti, and C. Majidi, *Soft and stretchable thermoelectric*

- generators enabled by liquid metal elastomer composites*. ACS applied materials & interfaces, 2020. **12**(15): p. 17921-17928.
71. Markvicka, E.J., et al., *An autonomously electrically self-healing liquid metal–elastomer composite for robust soft-matter robotics and electronics*. Nature materials, 2018. **17**(7): p. 618-624.
  72. Liu, H., et al., *Stimuli-Driven Insulator–Conductor Transition in a Flexible Polymer Composite Enabled by Biphasic Liquid Metal*. Advanced Materials, 2021. **33**(43): p. 2104634.
  73. Wang, H., et al., *A highly stretchable liquid metal polymer as reversible transitional insulator and conductor*. Advanced Materials, 2019. **31**(23): p. 1901337.
  74. Hajalilou, A., et al., *Biphasic Liquid Metal Composites for Sinter-Free Printed Stretchable Electronics*. Advanced Materials Interfaces, 2022. **9**(5): p. 2101913.
  75. Park, J., et al., *Liquid-metal embedded sponge-typed triboelectric nanogenerator for omnidirectionally detectable self-powered motion sensor*. Nano Energy, 2021. **89**: p. 106442.
  76. Saborio, M.G., et al., *Liquid metal droplet and graphene co-fillers for electrically conductive flexible composites*. Small, 2020. **16**(12): p. 1903753.
  77. Yun, G., et al., *Liquid metal-filled magnetorheological elastomer with positive piezoconductivity*. Nature communications, 2019. **10**(1): p. 1-9.
  78. Park, Y.G., et al., *Self-Healable, Recyclable Anisotropic Conductive Films of Liquid Metal-Gelatin Hybrids for Soft Electronics*. Advanced Electronic Materials, 2022. **8**(4): p. 2101034.
  79. Park, J.-E., et al., *Rewritable, printable conducting liquid metal hydrogel*. ACS nano, 2019. **13**(8): p. 9122-9130.
  80. Xu, J., et al., *Polymerization of moldable self-healing hydrogel with liquid metal*

- nanodroplets for flexible strain-sensing devices*. Chemical Engineering Journal, 2020. **392**: p. 123788.
81. Wang, M., et al., *Multifunctional Liquid-Free Ionic Conductive Elastomer Fabricated by Liquid Metal Induced Polymerization*. Advanced Functional Materials, 2021. **31**(32): p. 2101957.
  82. Yan, R., D. Gargas, and P. Yang, *Nanowire photonics*. Nature photonics, 2009. **3**(10): p. 569-576.
  83. Won, Y., et al., *A highly stretchable, helical copper nanowire conductor exhibiting a stretchability of 700%*. NPG Asia Materials, 2014. **6**(9): p. e132-e132.
  84. Chang, I., et al., *Bendable polymer electrolyte fuel cell using highly flexible Ag nanowire percolation network current collectors*. Journal of Materials Chemistry A, 2013. **1**(30): p. 8541-8546.
  85. Han, S., et al., *Nanorecycling: monolithic integration of copper and copper oxide nanowire network electrode through selective reversible photothermochemical reduction*. Advanced Materials, 2015. **27**(41): p. 6397-6403.
  86. Lee, H., et al., *Highly stretchable and transparent supercapacitor by Ag–Au core–shell nanowire network with high electrochemical stability*. ACS Applied Materials & Interfaces, 2016. **8**(24): p. 15449-15458.
  87. Lee, J., et al., *Room-temperature nanosoldering of a very long metal nanowire network by conducting-polymer-assisted joining for a flexible touch-panel application*. Advanced Functional Materials, 2013. **23**(34): p. 4171-4176.
  88. Yang, R., G. Chen, and M.S. Dresselhaus, *Thermal conductivity of simple and tubular nanowire composites in the longitudinal direction*. Physical Review B, 2005. **72**(12): p. 125418.
  89. Han, S., et al., *Fast plasmonic laser nanowelding for a Cu-nanowire percolation*

- network for flexible transparent conductors and stretchable electronics*. *Advanced materials*, 2014. **26**(33): p. 5808-5814.
90. Kim, K.K., et al., *Evolvable skin electronics by in situ and in operando adaptation*. *Advanced Functional Materials*, 2022. **32**(4): p. 2106329.
  91. Hong, S., et al., *Highly stretchable and transparent metal nanowire heater for wearable electronics applications*. *Advanced materials*, 2015. **27**(32): p. 4744-4751.
  92. Yeo, J., et al., *Flexible supercapacitor fabrication by room temperature rapid laser processing of roll-to-roll printed metal nanoparticle ink for wearable electronics application*. *Journal of Power Sources*, 2014. **246**: p. 562-568.
  93. Kim, K.K., et al., *A deep-learned skin sensor decoding the epicentral human motions*. *Nature communications*, 2020. **11**(1): p. 2149.
  94. Um, S.-H., et al., *Recent advances in selective laser-material interaction for biomedical device applications*. *Applied Physics Reviews*, 2022. **9**(4): p. 041302.
  95. Lin, T.-C., et al., *Aluminum with dispersed nanoparticles by laser additive manufacturing*. *Nature communications*, 2019. **10**(1): p. 1-9.
  96. Gusarov, A.V., et al., *On productivity of laser additive manufacturing*. *Journal of materials processing technology*, 2018. **261**: p. 213-232.
  97. Boulnois, J.-L., *Photophysical processes in recent medical laser developments: a review*. *Lasers in medical science*, 1986. **1**: p. 47-66.
  98. Ready, J.F., *Industrial applications of lasers*. 1997: Elsevier.
  99. Malinauskas, M., et al., *Ultrafast laser processing of materials: from science to industry*. *Light: Science & Applications*, 2016. **5**(8): p. e16133-e16133.
  100. Chen, J., et al., *Investigations on continuous-wave laser and pulsed laser induced controllable ablation of SiCf/SiC composites*. *Journal of the European Ceramic Society*, 2021. **41**(12): p. 5835-5849.

101. Gillner, A., et al., *Laser applications in microtechnology*. Journal of Materials Processing Technology, 2005. **167**(2-3): p. 494-498.
102. Yu, Y., et al., *Femtosecond laser-induced non-thermal welding for a single Cu nanowire glucose sensor*. Nanoscale Advances, 2020. **2**(3): p. 1195-1205.
103. Zhang, J., et al., *Femtosecond laser preparing patternable liquid-metal-repellent surface for flexible electronics*. Journal of Colloid and Interface Science, 2020. **578**: p. 146-154.
104. Kruth, J.-P., et al., *Lasers and materials in selective laser sintering*. Assembly Automation, 2003. **23**(4): p. 357-371.
105. Liu, S., et al., *Printed and Laser-Activated Liquid Metal-Elastomer Conductors Enabled by Ethanol/PDMS/Liquid Metal Double Emulsions*. ACS Applied Materials & Interfaces, 2021. **13**(24): p. 28729-28736.
106. Liu, S., et al., *Oxide rupture-induced conductivity in liquid metal nanoparticles by laser and thermal sintering*. Nanoscale, 2019. **11**(38): p. 17615-17629.
107. Russo, R.E., et al., *Laser ablation*, in *Laser-induced breakdown spectroscopy*. 2007, Elsevier. p. 41-70.
108. Lu, T., et al., *Soft-matter printed circuit board with UV laser micropatterning*. ACS applied materials & interfaces, 2017. **9**(26): p. 22055-22062.
109. Lim, J., et al., *Monolithic digital patterning of polyimide by laser-induced pyrolytic jetting*. Chemical Engineering Journal, 2022. **428**: p. 131050.
110. Shin, J., et al., *Monolithic digital patterning of polydimethylsiloxane with successive laser pyrolysis*. Nature Materials, 2021. **20**(1): p. 100-107.
111. Gu, D.D., et al., *Laser additive manufacturing of metallic components: materials, processes and mechanisms*. International materials reviews, 2012. **57**(3): p. 133-164.
112. Gorte, B. and N. Pfeifer, *Structuring laser-scanned trees using 3D mathematical*

- morphology*. International Archives of Photogrammetry and Remote Sensing, 2004. **35**(B5): p. 929-933.
113. Gower, M.C., *Industrial applications of laser micromachining*. Optics express, 2000. **7**(2): p. 56-67.
114. Selimis, A., V. Mironov, and M. Farsari, *Direct laser writing: Principles and materials for scaffold 3D printing*. Microelectronic Engineering, 2015. **132**: p. 83-89.
115. Shin, J., et al., *Sensitive wearable temperature sensor with seamless monolithic integration*. Advanced Materials, 2020. **32**(2): p. 1905527.
116. Park, S., et al., *Fully laser-patterned stretchable microsupercapacitors integrated with soft electronic circuit components*. NPG Asia Materials, 2018. **10**(10): p. 959-969.
117. Ye, R., D.K. James, and J.M. Tour, *Laser-induced graphene*. Accounts of chemical research, 2018. **51**(7): p. 1609-1620.
118. Thakur, A.K., et al., *Laser-induced graphene–PVA composites as robust electrically conductive water treatment membranes*. ACS applied materials & interfaces, 2019. **11**(11): p. 10914-10921.
119. McDonald, J.C. and G.M. Whitesides, *Poly (dimethylsiloxane) as a material for fabricating microfluidic devices*. Accounts of chemical research, 2002. **35**(7): p. 491-499.
120. Tabor, C., S. Holcomb, and J. Heikenfeld, *Reliable and Reversible Contact of Eutectic Gallium Indium and Copper Electrodes*. Advanced Materials Interfaces, 2020. **7**(15): p. 1902182.
121. Zavabeti, A., et al., *A liquid metal reaction environment for the room-temperature synthesis of atomically thin metal oxides*. Science, 2017. **358**(6361): p. 332-335.

122. Li, J. and L. Zhang, *Study of desiccation crack initiation and development at ground surface*. Engineering Geology, 2011. **123**(4): p. 347-358.
123. Jensen, W.B., *The origins of the Hirsch and Büchner vacuum filtration funnels*. Journal of Chemical Education, 2006. **83**(9): p. 1283.
124. Zhang, S., Y. Li, and N. Pan, *Graphene based supercapacitor fabricated by vacuum filtration deposition*. Journal of Power sources, 2012. **206**: p. 476-482.
125. Boley, J.W., E.L. White, and R.K. Kramer, *Mechanically sintered gallium-indium nanoparticles*. Adv Mater, 2015. **27**(14): p. 2355-60.
126. Isichenko, M.B., *Percolation, statistical topography, and transport in random media*. Reviews of modern physics, 1992. **64**(4): p. 961.
127. Harrison, R.L. *Introduction to monte carlo simulation*. in *AIP conference proceedings*. 2010. American Institute of Physics.
128. Rezaie, K., et al., *Using extended Monte Carlo simulation method for the improvement of risk management: Consideration of relationships between uncertainties*. Applied Mathematics and Computation, 2007. **190**(2): p. 1492-1501.
129. Glickman, E., et al., *Interaction of liquid and solid gallium with thin silver films: Synchronized spreading and penetration*. Acta materialia, 2011. **59**(3): p. 914-926.
130. Ni, X., et al., *Monte Carlo simulations of electrical percolation in multicomponent thin films with nanofillers*. Nanotechnology, 2018. **29**(7): p. 075401.
131. Yao, H., et al., *Modelling electrical conduction in nanostructure assemblies through complex networks*. Nature Materials, 2020. **19**(7): p. 745-751.
132. Pike, G. and C. Seager, *Percolation and conductivity: A computer study. I*. Physical review B, 1974. **10**(4): p. 1421.
133. Englman, R., Z. Jaeger, and A. Levi, *Percolation theoretical treatment of two-dimensional fragmentation in solids*. Philosophical Magazine B, 1984. **50**(2): p.

- 307-315.
134. Charlaix, E., E. Guyon, and N. Rivier, *A criterion for percolation threshold in a random array of plates*. Solid state communications, 1984. **50**(11): p. 999-1002.
  135. Robinson, P., *Numerical calculations of critical densities for lines and planes*. Journal of Physics A: Mathematical and General, 1984. **17**(14): p. 2823.
  136. Dittlacher, H., et al., *Silver nanowires as surface plasmon resonators*. Phys Rev Lett, 2005. **95**(25): p. 257403.
  137. Roper, D.K., W. Ahn, and M. Hoepfner, *Microscale heat transfer transduced by surface plasmon resonant gold nanoparticles*. The Journal of Physical Chemistry C, 2007. **111**(9): p. 3636-3641.
  138. Shin, J., et al., *Monolithic digital patterning of polydimethylsiloxane with successive laser pyrolysis*. Nat Mater, 2021. **20**(1): p. 100-107.
  139. Deng, B. and G.J. Cheng, *Pulsed Laser Modulated Shock Transition from Liquid Metal Nanoparticles to Mechanically and Thermally Robust Solid-Liquid Patterns*. Adv Mater, 2019. **31**(14): p. e1807811.
  140. Lopes, P.A., et al., *Bi-Phasic Ag-In-Ga-Embedded Elastomer Inks for Digitally Printed, Ultra-Stretchable, Multi-layer Electronics*. ACS Appl Mater Interfaces, 2021. **13**(12): p. 14552-14561.
  141. Jasper, W.J. and N. Anand, *A generalized variational approach for predicting contact angles of sessile nano-droplets on both flat and curved surfaces*. Journal of Molecular Liquids, 2019. **281**: p. 196-203.
  142. Berini, P. and I. De Leon, *Surface plasmon–polariton amplifiers and lasers*. Nature photonics, 2012. **6**(1): p. 16-24.
  143. Reineck, P., et al., *UV plasmonic properties of colloidal liquid-metal eutectic gallium-indium alloy nanoparticles*. Scientific reports, 2019. **9**(1): p. 5345.

144. Park, J.H., et al., *Plasmonic-tuned flash Cu nanowelding with ultrafast photochemical-reducing and interlocking on flexible plastics*. *Advanced Functional Materials*, 2017. **27**(29): p. 1701138.
145. Chen, Z., et al., *Imaging local heating and thermal diffusion of nanomaterials with plasmonic thermal microscopy*. *ACS nano*, 2015. **9**(12): p. 11574-11581.
146. Park, J.E., et al., *Autonomous Surface Reconciliation of a Liquid-Metal Conductor Micropatterned on a Deformable Hydrogel*. *Adv Mater*, 2020. **32**(37): p. e2002178.
147. Dickson, L.D., *Characteristics of a propagating Gaussian beam*. *Applied Optics*, 1970. **9**(8): p. 1854-1861.
148. Kim, M., et al., *Nanowire-assisted freestanding liquid metal thin-film patterns for highly stretchable electrodes on 3D surfaces*. *npj Flexible Electronics*, 2022. **6**(1): p. 99.
149. Won, D., et al., *Digital selective transformation and patterning of highly conductive hydrogel bioelectronics by laser-induced phase separation*. *Science Advances*, 2022. **8**(23): p. eabo3209.
150. Chen, B., et al., *Liquid Metal-Tailored PEDOT: PSS for Noncontact Flexible Electronics with High Spatial Resolution*. *ACS nano*, 2022. **16**(11): p. 19305-19318.

## 국문 초록

# 액체 금속과 금속 나노와이어 기반 가변적 전기적 물성을 가진 레이저 유도 금속성 2상 복합체

서울대학교 대학원  
기계공학부  
조철민

근래들어 광범위한 과학 기술의 발전 덕분에 바이오, 에너지, 소프트 로봇 등 다양한 어플리케이션에 광범위하게 활용 가능한 스트레처블 일렉트로닉스가 활발히 연구되고 있다. 스트레처블 일렉트로닉스의 근간이 되는 스트레처블 전극은 다양한 소재 및 공정적 관점에서 집중적으로 연구가 되는 한편, 이를 기반한 인간 삶에 도움이 될 수 있는 새로운 어플리케이션들 또한 계속 보고되고 있다.

본 학위논문에서는 재료적 관점에서 액체 금속과 나노 와이어를, 그리고 공정적 관점에서 레이저를 선정하여 스트레처블 전극을 개발한 것을 보고한다. 기존 연구들이 액체 금속과 나노 와이어의 한 속성만을 이용하였다면, 본 학위 논문에서는 액체 금속이 지니고 있는 특유의 액체적 성질과 나노 와이어의 1D 물질로서 전도성 구조체를 이룰 수 있는 성질을 조합하여, 레이저 장비를 통해 원하는 영역만 두 물질의 얽힘의 정도를 조절시켰다. 이로부터 전기적 물성이 조절 가능한 금속성

2상 (고체-액체) 복합체를 개발하여 히터로서 그 활용 가능성을 확인하였다. 한편, 균일한 성능을 가진 동일 전극을 제작하기 위하여 본 학위논문에서 새롭게 고안된 감압여과 방식 필름 제작 및 이에 관련된 시뮬레이션 연구는 향후 다른 연구자들에게 본 연구에 근간한 새로운 연구를 위한 좋은 밑거름이 될 것이다.

**주요어:** 액체 금속  
금속 나노와이어  
레이저  
신축성 전극  
금속성 2상 복합체  
가변 물성

**학 번:** 2019-35256